Uplift Resistance of Anchor Plate Using Extended Mohr-Coulomb Model

Kyeong Sun Kim

Civil and Environmental Engineering

Seoul National University

November, 2021

Contents

Contents

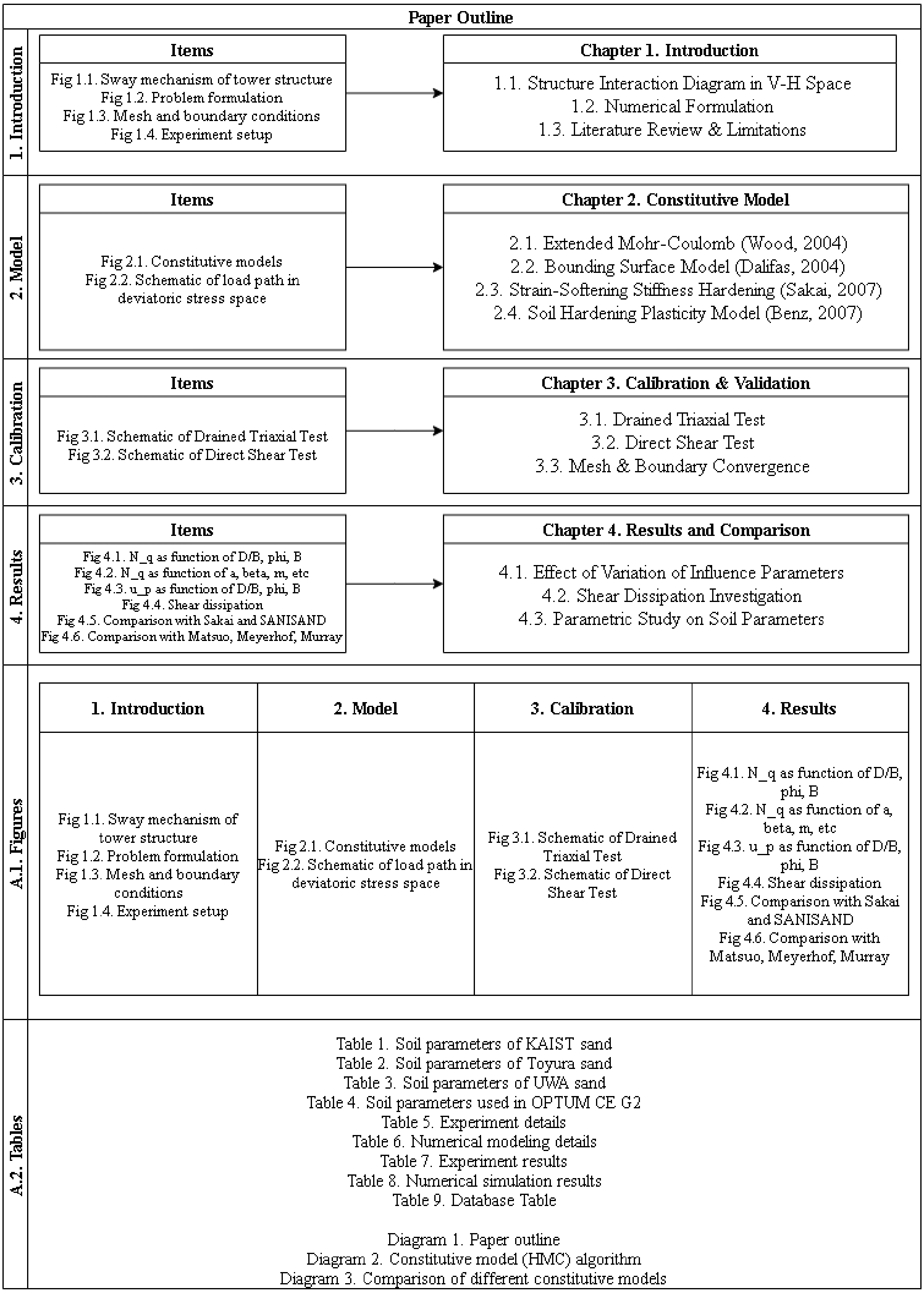

Figure 1: Paper Outline

1

Constitutive Model

Contents

Here is a brief description of the constitutive models:

1. Strain—Softening Stiffness—Hardening Model by Sakai and Tanaka, 1993
2. Typical Mohr-Coulomb with Non-associated Flow
3. Extended Mohr-Coulomb Model by David Muir Wood, 2004

1.1 Strain—Softening Stiffness—Hardening Model

It is assumed that the yield function F is defined by the stress $\vec{\sigma}$ and the soil parameter χ (Tanaka and Sakai, 1993):

$F(\vec{\sigma}, \alpha(\chi)) \;=\; 0$

In order to avoid numerical instability due to singularity of the non-associated Mohr-Coulomb model, a constitutive model based on the yield function of M-C type and the plastic potential function of Draker-Prager type is employed.

For predicting deformations in a post-peak regime, the elastic- strain-softening plastic model is developed. The yield function is given by the following expression.

1.1.1 Yield function

$$F(\vec{\sigma}, \alpha(\chi)) = 3\alpha(\chi)p' + \frac{\sqrt{J_2}}{g(\theta)} - c(\chi) = 0$$

1.1.2 Plastic potential function

$$G(\vec{\sigma}, \alpha'(\chi)) = 3\alpha^{'}(\chi)p' + \sqrt{J_2} - c(\chi) = 0$$

$$\chi = \int \delta\varepsilon^p$$

$$(\delta\varepsilon^p)^2 = 2[(\delta\epsilon_x^p)^2 + (\delta\epsilon_y^p)^2 + (\delta\epsilon_z^p)^2 +] + (\delta\gamma^p)^2$$

, where

$p^{'}$ is mean stress,

J_2 is second invariant of deviatoric stress,

χ is soil hardening parameter,

$c(\chi)$ is apparent cohesion function,

$\delta\varepsilon^p_{x,y,z}, \delta\gamma^p$ is incremental deviatoric plastic strains.

In case of the Mohr-Coulomb model, $g(\theta)$ is given by:

$$g(\theta) = \frac{3 - sin\phi}{2\sqrt{3}cos\theta - 2sin\theta sin\phi}$$

, where

θ is Lode angle; if triaxial compression, $= -30°$

ϕ is mobilized internal friction angle.

1.1.3 Hardening function

The simple strain-softening functions are specified and expressed as a function of material constants. (Tanaka and Sakai, 1993)

$$\alpha(\chi) = (\frac{2\sqrt{a\chi}}{\chi + a})^m \alpha_p(hardening\, regime;\ \chi \leq a)$$

$$\alpha(\chi) = \alpha_r + (\alpha_p - \alpha_r)exp\{-(\frac{\chi - a}{b})\}(softening\, regime;\ \chi > a)$$

, where

a, b, m are soil parameters.

Similar expressions are used by de Borst (1986).

$$\alpha_p = \frac{2sin\phi_p}{\sqrt{3}(3 - sin\phi_p)}$$

$$\alpha_r = \frac{2sin\phi_r}{\sqrt{3}(3 - sin\phi_r)}$$

, where

$\phi_{p,r}$ are peak and residual friction angle, respectively.

1.2 Nonassociated Flow Rule (NA)

Since there may be a range of possible solutions, each associated with a different pattern of localization and all of which are entirely valid, it can be expected that any numerical solution will be very sensitive to both physical imperfections as well as round-off errors and the exact sequence in which the procedures defining the solution scheme are carried out. In the end, the result is a load-displacement response that tends to be rather oscillatory.

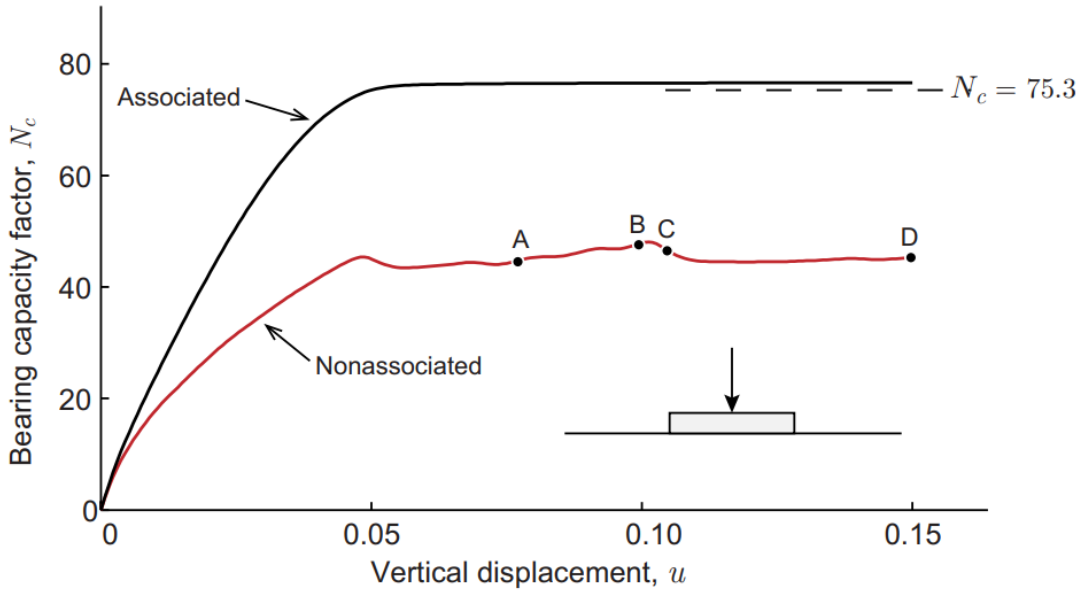

Figure 1.1: Load-displacement response for strip footing on a weightless soil (After Krabbenhoft et al., 2012)

The basic idea behind the formulation derives from the structure of the internal dissipation associated with constitutive models. Let us assume a yield function of the type:

$$F = Mp + q - c$$

, where

p and q are mean and deviatoric stress, M is a friction coeffcieint, and c is cohesion.

The plastic potential function is given by:

$$G = Np + q$$

, where $N \leq M$ is a dilation coefficient.

In $p - q$ triaxial space, the plastic strain rates are given by:

$$\delta\varepsilon_v^p = \delta\lambda\frac{\partial G}{\partial p} = \delta\lambda N \delta\varepsilon_s^p = \delta\lambda\frac{\partial G}{\partial p} = \delta\lambda$$

, where δ denotes time increment, ε_v^p and ε_s^p are volumetic and deviatoric plastic strains conjugate to p and q, respectively.

The dissipation D is given by:

$$\begin{aligned} D &= p\varepsilon_v^p + q\varepsilon_s^p \\ &= (Nq + q)\delta\lambda \\ &= [c - (M - N)p]\delta\lambda \\ &= [c - (M - N)p]\varepsilon_s^p \end{aligned}$$

The above-mentioned parameters are all related with the confining pressure, which can be easily illustraed with the figure below:

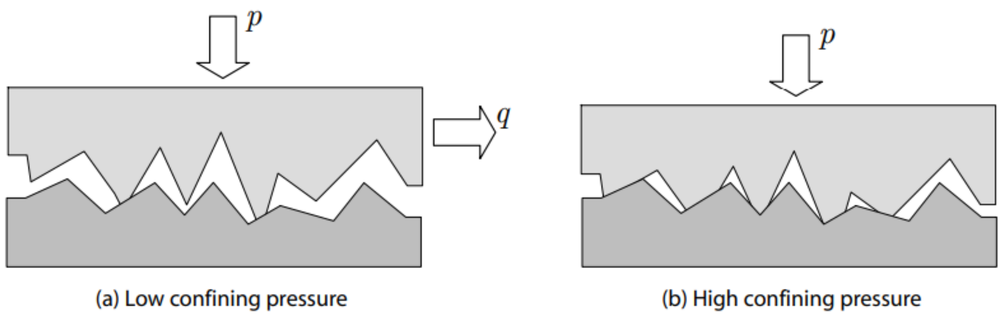

Figure 1.2: Microscopic origins of friction as plastic shearing of asperities. A higher confining pressure implies a higher degree of interlocking of the asperities and thereby a higher apparent shear strength (After Krabbenhoft et al., 2012)

1.3 Extended Mohr—Coulomb Model (EMC)

The elastic-perfectly plastic Mohr-Coulomb model is widely used for geotechnical analysis. It provides very crude match to actual shearing behavior of soils. A natural extension is to create a hardening version of the M-C model in which the size of the yield surface varies in some nonlinear way with the development of plastic strain. In the model to be described as hardening will be linked only with distortional strain. It is useful for modelling sands , where it is rearrangement of the rather particles that dominates the response and irrecoverable volumetric changes are essentially linked by this rearrangement of particles (Wood, 2004).

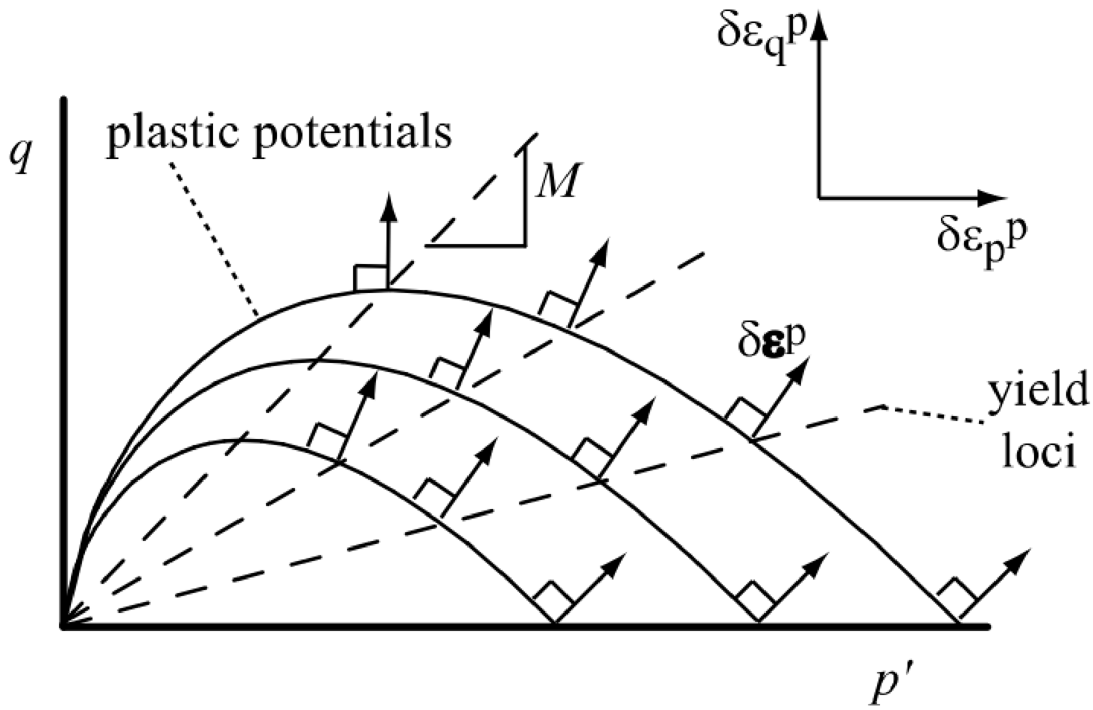

Figure 1.3: Plastic potential curves (solid lines) and yield loci (dashed lines) in elastic-hardening plastic Mohr-Coulomb modele

Following Taylor's (1948) proposal of a link between dilatancy and mobilized friction in a shear box test, stress—dilatancy equation expressed in terms of total strain increments is obtained.

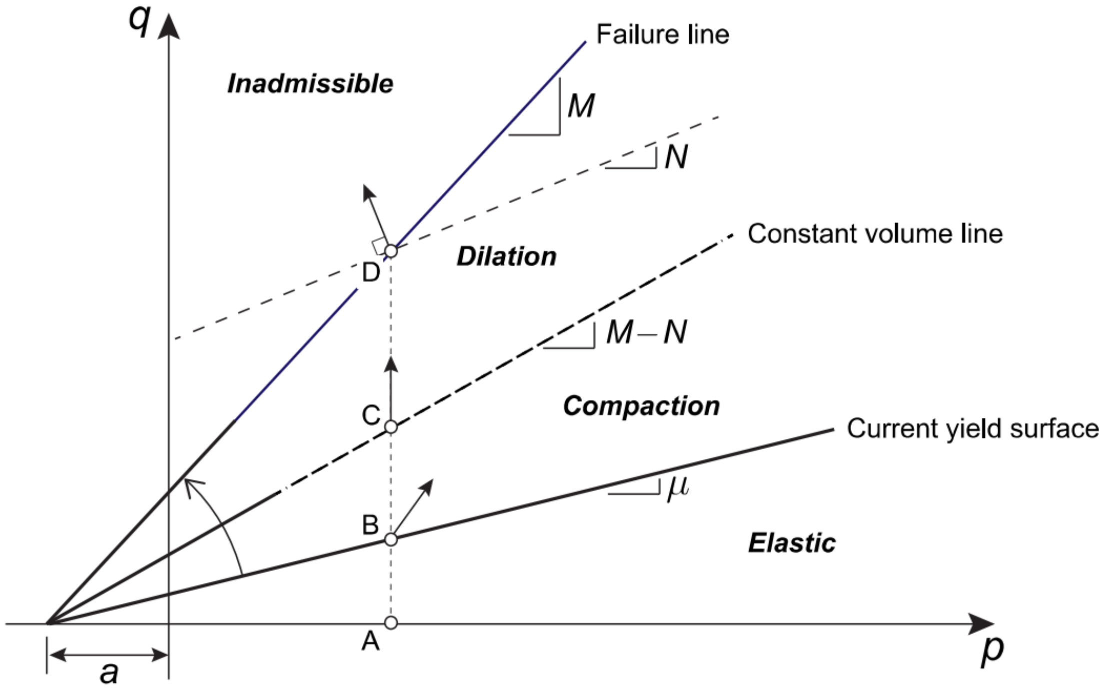

Figure 1.4: Hardening, compaction and dilation in the HMC model

1.3.1 Comparison between associated and non-associated flow rule in plastic model

In the elastic-perfectly-plastic Mohr-Coulomb model, it is commonly assumed that the plastic potential takes the same form as the yield surface, but with the slope defined by a dilation angle ψ rather than a friction angle. If this assumption is adopted, then the dirction of the plastic strain increment $\delta\varepsilon^p$ would be normal to a set of parallel lines by the dilation angle. If normality rule were assumed, radical difference between the slope of yield criterion line and the plastic potental contour is observed (J.P. Doherty and D. Muir Wood, 2013).

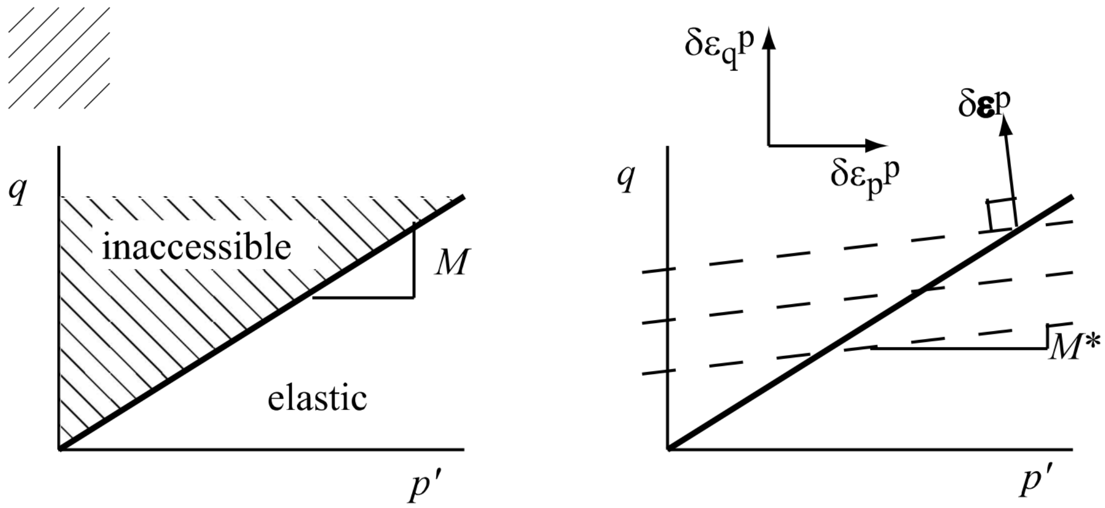

Figure 1.5: Elastic-perfectly plastic Mohr-Coulomb model (a) yield and failure locus, (b) plastic potentials

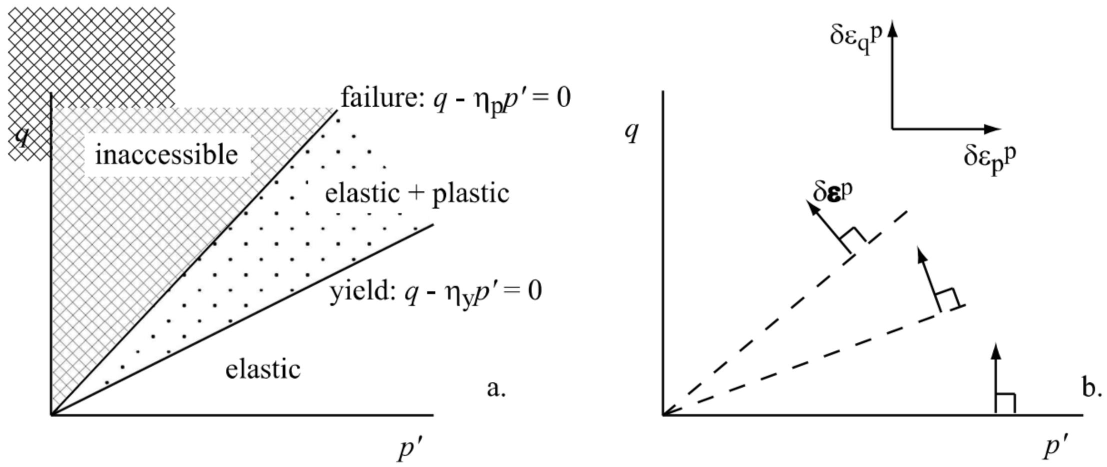

Figure 1.6: Elastic-hardening plastic Mohr-Coulomb model (a) yield locus and failure locus separating elastic plastic and inaccessible regions of stress plane (b) normality applied at the plastic region

1.3.2 Yield function

$$F(\vec{\sigma}, \chi) = F(p', q, \chi) = q - \eta_y p' = 0$$

1.3.3 Plastic potential function

$$G(\vec{\sigma}) = q - (M - M')p' ln(\frac{p'_r}{p'}) = 0$$

, where $\eta_{y,p}$ is stress ratio at yield and peak, respectively,

p'_r is chosen s.t. plastic potential gradient passes through current stress, i.e.,

$p'_r = p' exp\{\frac{\eta_y}{M-M'}\}$

M is material parameter at perfect plasticity when hardening terminates.

$M = \frac{6sin\phi}{3-sin\phi}$

M' is dilation at constant volume line:

$M' = \frac{6sin\psi}{3-sin\psi}$

$M' = M - k\psi = M - k(v - \Gamma + \lambda ln p')$

k is soil constant linking state variable and strength.

Critical State description is as follows:

$M' = M - k[(v_0 - \Gamma + \lambda ln p'_0 + (\lambda ln \frac{p'}{p'_0} - v_0 \varepsilon^e_p) - v_0 \varepsilon^p_p)].$

1.3.4 Flow rule

$$\frac{\delta\varepsilon^p_p}{\delta\varepsilon^p_q} = M - M' - \eta_y$$

1.3.5 Hardening

$$\delta\eta_y = \frac{1 - \frac{\eta_y}{M}}{\beta}\delta\varepsilon^p_q$$

, where

β is a model parameter scaling plastic strain,

$\beta = \frac{3}{2}p' \frac{9-M}{9-(M-M')Mln2-3M'} \frac{1-E_{50}/E_{ur}}{E_{50}}$ for Taylor's $\sigma - \psi$ relation.

The incremental of the stress ratio is defined as:

$\delta\eta_y = \frac{3sin\delta\phi}{\sqrt{3}cos\theta + sin\theta sin\delta\phi}$

1.3.6 Soil Parameters

Elastic Moduli

The elastic moduli are estimated from the modified equation proposed by Hardin and Black (1968) in the case of sand:

$$G = G_0 \frac{(2.17-e)^2}{1+e} \sqrt{p'} K = \frac{1+\nu}{3(1-2\nu)} G$$

, where

ν is Poisson's ratio,

e is void ratio,

G_0 is initial shear modulus.

Peak friction angle

The peak friction angle of ϕ_p is estimated from the empirical relations proposed by Bolton (1987):

$$I_r = D_r[5 - ln(\frac{p'}{150})] - 1,\ (p' \geq 150kN/m^2) I_r = 5D_r - 1,\ (p' < 150kN/m^2) \phi_p = 3I_r + \phi_r$$

Dilatency angle

The dilatency angle of ψ is estimated from modified Rowe's stress–dilatency relationship:

$$sin\psi = \frac{sin\phi - sin\phi'_r}{1 - sin\phi sin\phi'_r} \phi'_r = \phi_r[1 - \beta exp\{-(\frac{\chi}{\epsilon_d})^2\}]$$

, where

β and ϵ_d are stress—dilatency material parameters.

E_{50} is a secant modulus defined as:

$E_{50} = \frac{\frac{1}{2}q_u}{\varepsilon_{a,50}}$

E_{ur} is unloading/reloading stiffness.

2

Calibration and Validation

Contents

For the validity of the finite element tests performed, the triaxial elemental test is siumlated with the box of union length. The set up is as follows:

2.1 Drained Triaxial Test

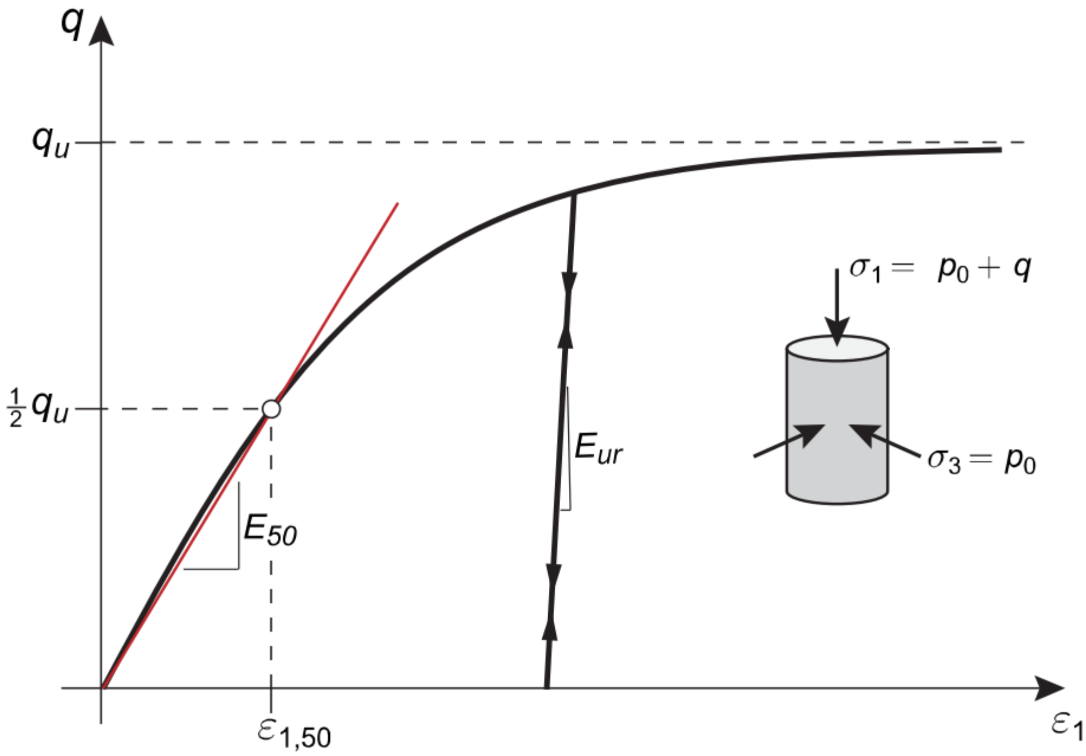

Figure 2.1: Typical triaxial test (After Krabbenhoft, 2013)

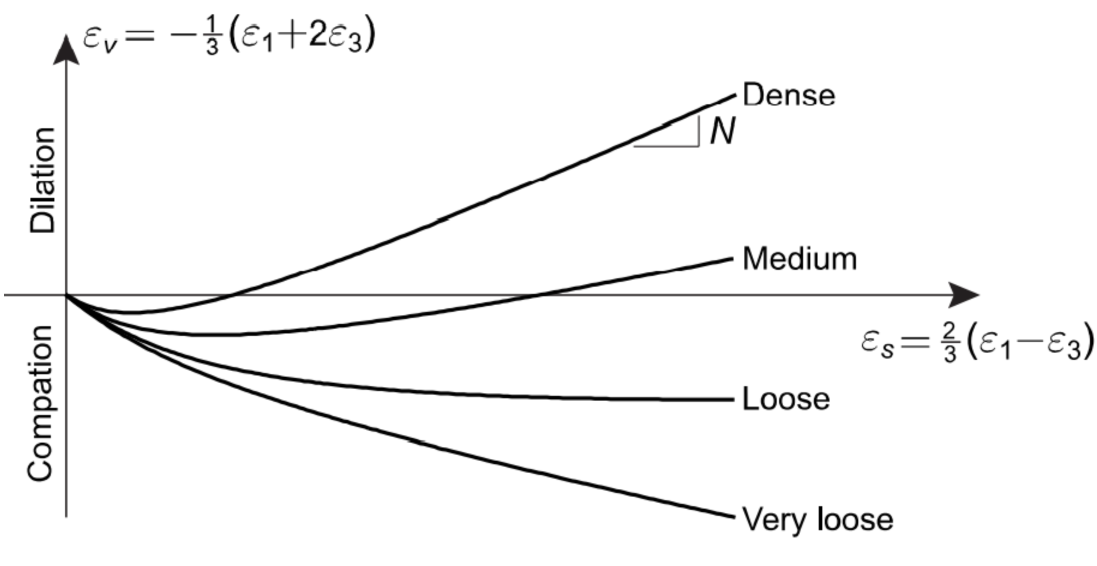

Figure 2.2: Typical shear-volumetric strain behavior in triaxial compression (After Krabbenhoft, 2013)

Two tests — Triaxial compression and extension (TC/TE) — are simulated using Multiplier Elasto—plastic analysis under axisymmetric conditions as indicated in the Figure below. The fixed loads here represent the initial axial and radial stresses while the axial Multiplier load is increased in the course of the analysis to reach the ultimate limit state.

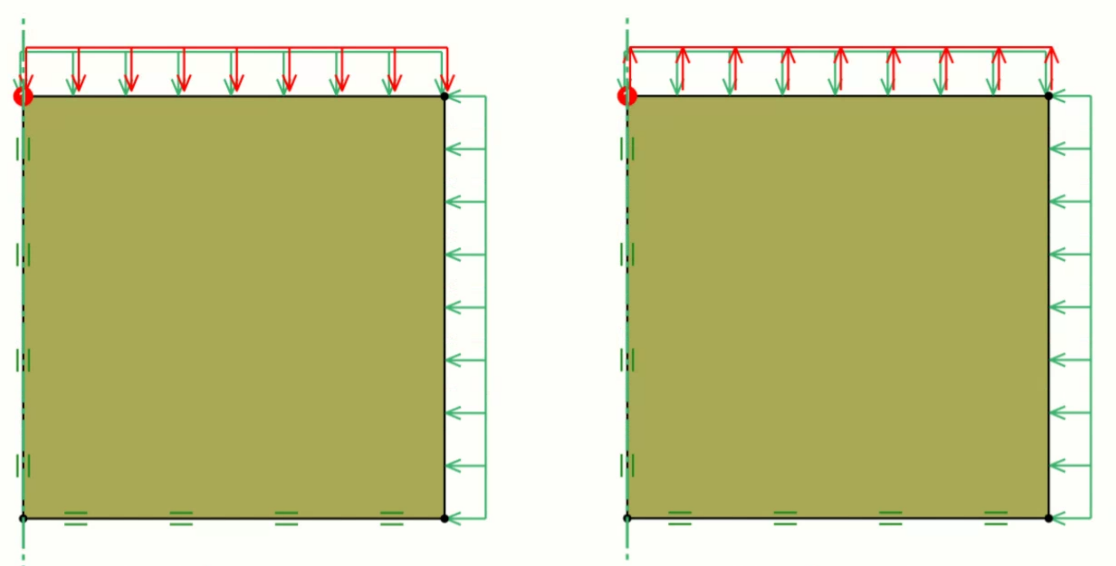

Figure 2.3: Setup for elemental triaxial compression and extension

By a process of trial and error, the fits shown in Figure are obtained. For this data set , where no information about the behavior in simple shear is available the value is well within range that can be accommodated by the isotropic strength option, there is little reason to assume any anisotropy. We note that the compression secant modulus in compression is only half of the extension secant modulus. This is somewhat unusual, but in this case nevertheless what fits the data best.

Result of Elemental Triaxial Test at 100 kPa

Triaxial test at radial stress of 100 kPa is simulated using one by one block of the finite elmeent formulation with the EMC model.

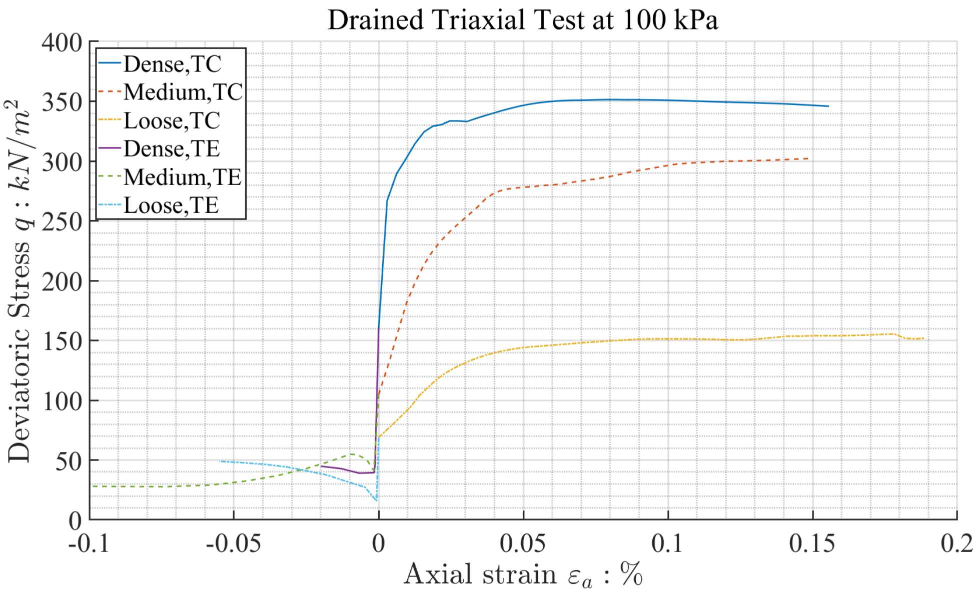

Figure 2.4: Result of Drained Triaxial test at 100 kPa

Result of Elemental Triaxial Test at 200 kPa

Triaxial test at radial stress of 200 kPa is simulated using one by one block of the finite elmeent formulation with the EMC model.

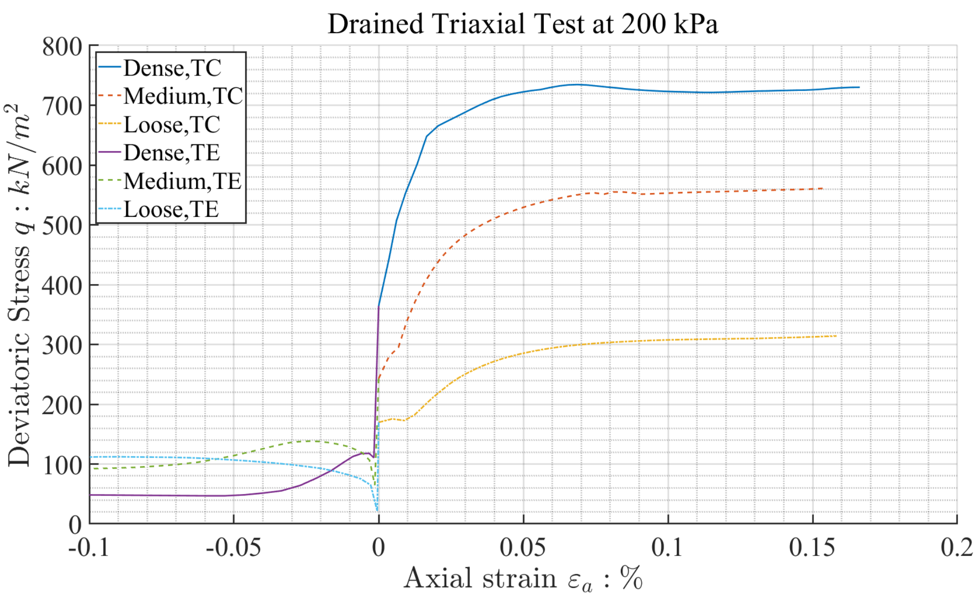

Figure 2.5: Result of Drained Triaxial test at 200 kPa

2.2 Soil Parameters

2.2.1 Strain—Softening Stiffness—Hardening Model

Here is a table presenting the model parameters used by Sakai and Tanaka (1993).

Parameters	Loose	Medium	Dense
Density $\gamma(kN/m3)$	13.5	14.8	16.3
Void ratio e	0.95	0.78	0.62
Relative density D_r	0.05	0.53	0.95
Coefficient of shear modulus, G_0	500	500	500
Poisson's ratio, ν	0.3	0.3	0.3
Peak friction angle, $\phi_p(°)$	33	38	45
Residual friction angle, $\phi_r(°)$	33	33	33
Dilation angle, $\psi(°)$	0	10	20
Shear band thickness, $S.B.(cm)$	0.3	0.3	0.3
Soil parameter, a	0.1	0.1	0.1
Soil parameter, b	0.8	0.4	0.1
Soil parameter, ε_d	0.3	0.3	0.3
Soil parameter, m	0.4	0.2	0.1
Soil parameter, β	0.1	0.1	0.1

Table 2.1: Model parameters used by Sakai and Tanaka, 1993

2.2.2 Nonassociated Flow Rule (NA)

Here is a table presenting the model parameters used in Nonassociated (NA) simulations.

Parameter	Dense	Medium	Loose
$E(MPa)$	50	25	15
ν	0.3	0.25	0.2
$c(kPa)$	0	0	0
$\phi(°)$	40	35	30
$\psi(°)$	10	5	0
$\gamma_{dry}(kN/m^3)$	18	16	14
$\gamma_{sat}(kN/m^3)$	21	20	19
K_0	0.3572	0.4264	0.5

Table 2.2: Soil parameters used in nonassociated flow (NA) simulations

2.2.3 Extended Mohr—Coulomb Model (EMC)

Here is a table presenting the model parameters used in Extended Mohr-Coulomb (EMC) simulations.

Parameter	Dense	Medium	Loose
$E_{50}(MPa)$	50	25	13
$E_{ur}(MPa)$	150	75	39
ν_{ur}	0.4	0.35	0.3
$c(kPa)$	0	0	0
$\phi(°)$	41	37	27
$\psi(°)$	17	11	-4
$\gamma_{dry}(kN/m^3)$	18	16	14
$\gamma_{sat}(kN/m^3)$	21	20	19
K_0	0.3572	0.4264	0.5
$p_{ref}(kPa)$	100	100	100
Soil parameter, m	0.5	0.5	0.5

Table 2.3: Soil parameters used in Extended Mohr-Coulomb Model (EMC)simulations

2.3 Convergence Criteria

2.3.1 Mesh Convergence

Here is a table presenting the result of mesh convergence test on both NA and EMC models.

The goal of the mesh convergence test usually is to seek the acceptable range of number of the mesh size. However, the interest in the present paper differs from the previously investigated objectives, in a way that the object sought is not the same. The present paper seeks to draw a more detailed analysis of the failure surface formed as the soil is sheared.

Some authors in the past described this with the width of the shear band (Tanaka and Sakai, 1993). However, the present paper deals only with the limit analysis formulation using the Extended Mohr-Coulomb model.

Type of Analysis	Mesh Number	$p_u, kN/m2$	Variance	Std
Non-associated (NA)	250	137.7	0.11	0.33
Non-associated (NA)	500	135.8	1.23	1.11
Non-associated (NA)	1000	129.4	13.85	3.72
Non-associated (NA)	2000	139.8	0.28	0.52
Non-associated (NA)	5000	138.2	0.02	0.13
Non-associated (NA)	10000	141.7	1.69	1.30
Non-associated (NA)	20000	147	12.00	3.46
Extened Mohr-Coulomb (EMC)	250	161.3	1.51	1.23
Extened Mohr-Coulomb (EMC)	500	159.6	0.29	0.54
Extened Mohr-Coulomb (EMC)	1000	161.4	1.62	1.27
Extened Mohr-Coulomb (EMC)	2000	158.4	0.00	0.05
Extened Mohr-Coulomb (EMC)	5000	157.3	0.16	0.40
Extened Mohr-Coulomb (EMC)	10000	156.2	0.73	0.85
Extened Mohr-Coulomb (EMC)	20000	153.8	3.35	1.83

Table 2.4: Setup and result of mesh convergence test

Mesh Convergence Results

The reulst of the present investigation is the determination of the number of the mesh elements be around 2000.

However, it is noted that further studies, outside of this paper, is onto the maximum number of the elements to be studied, for this will enhance the visualization of the shear band formation, as well as the guidance onto the study of the shear dissipation.

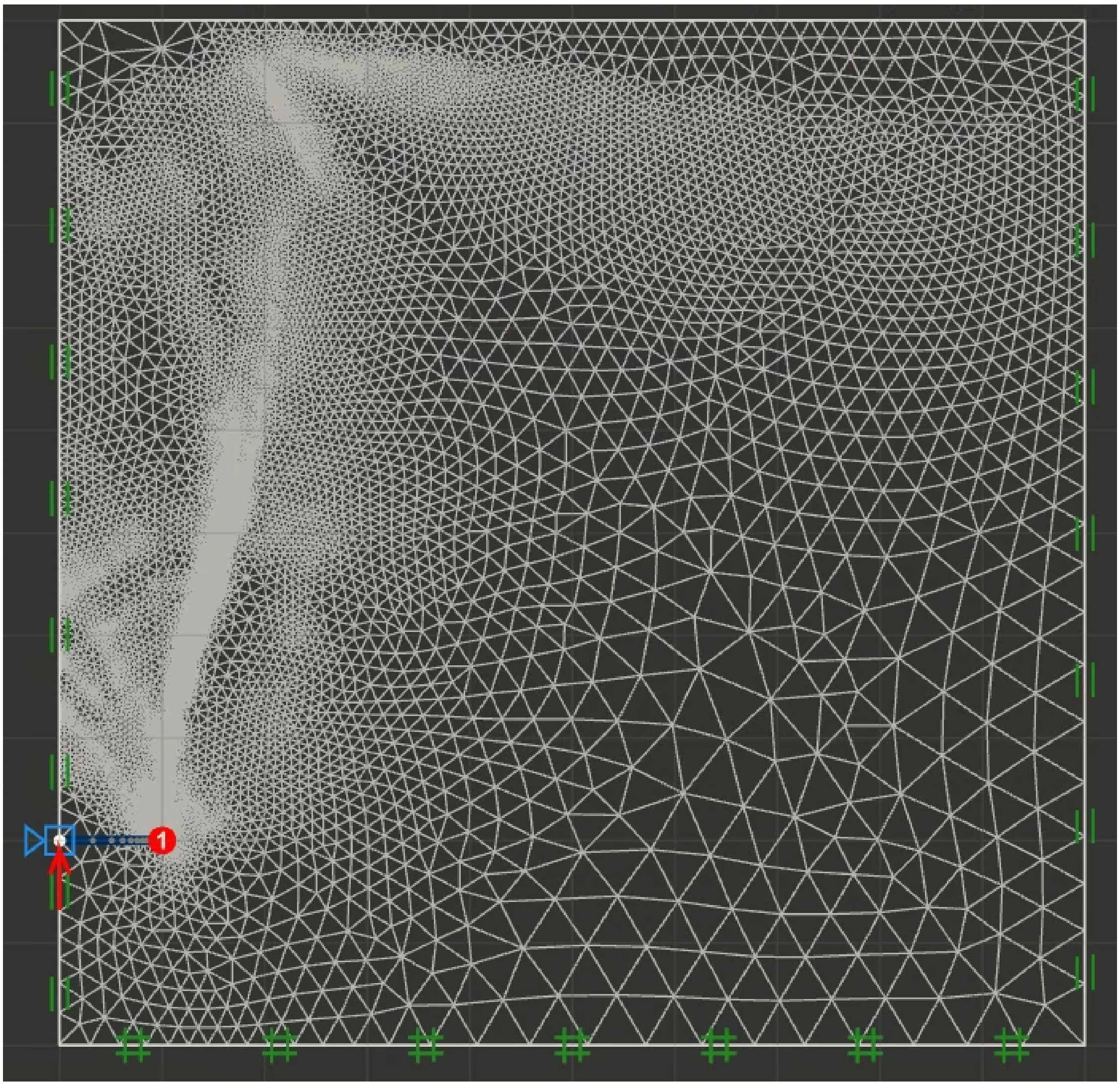

Figure 2.6: Typical result from mesh convergence test (maximum number of elements)

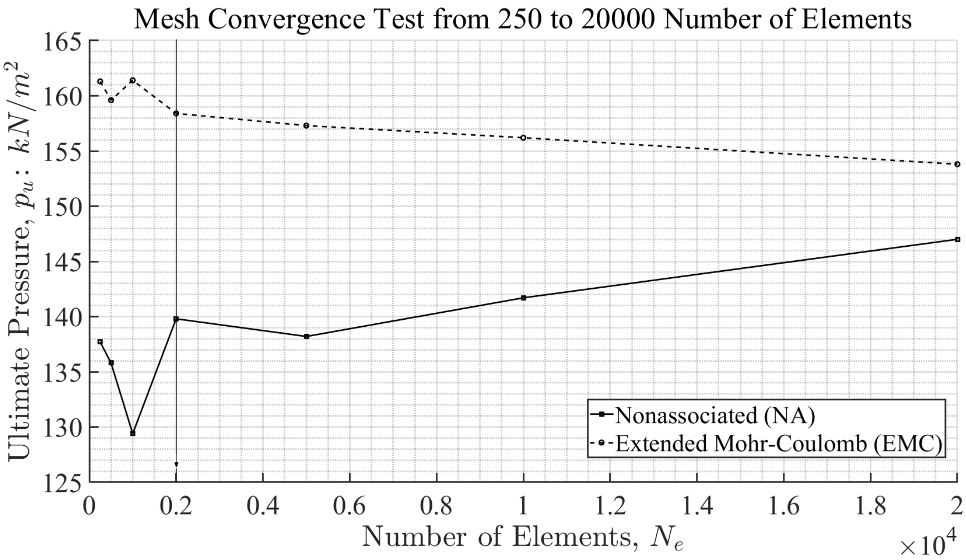

Figure 2.7: Result of the mesh convergence test, which confirms that about 2000 elements are acceptable

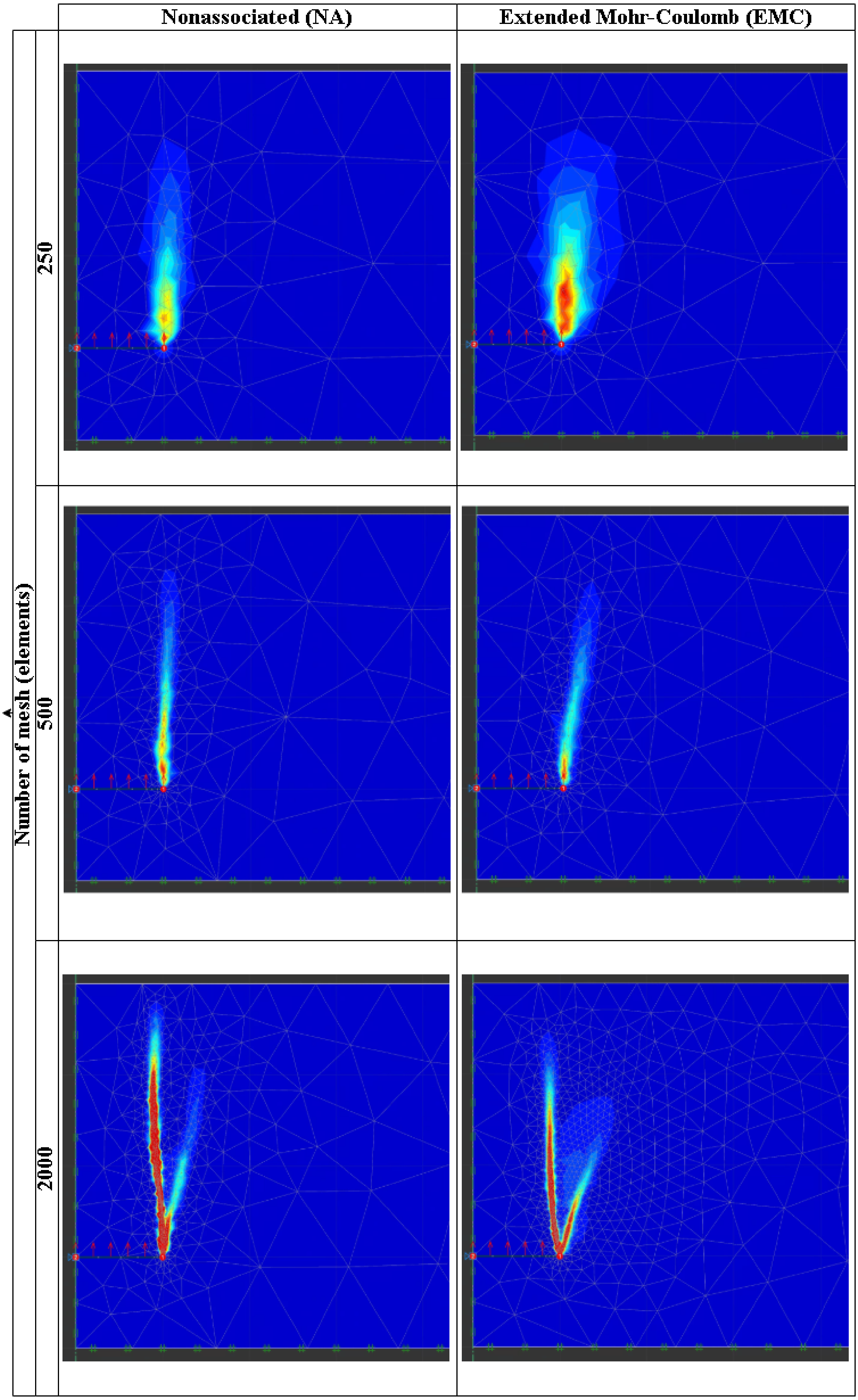

Figure 2.8: Shear Dissipation of the mesh convergence test of 250, 500, 2000 elements

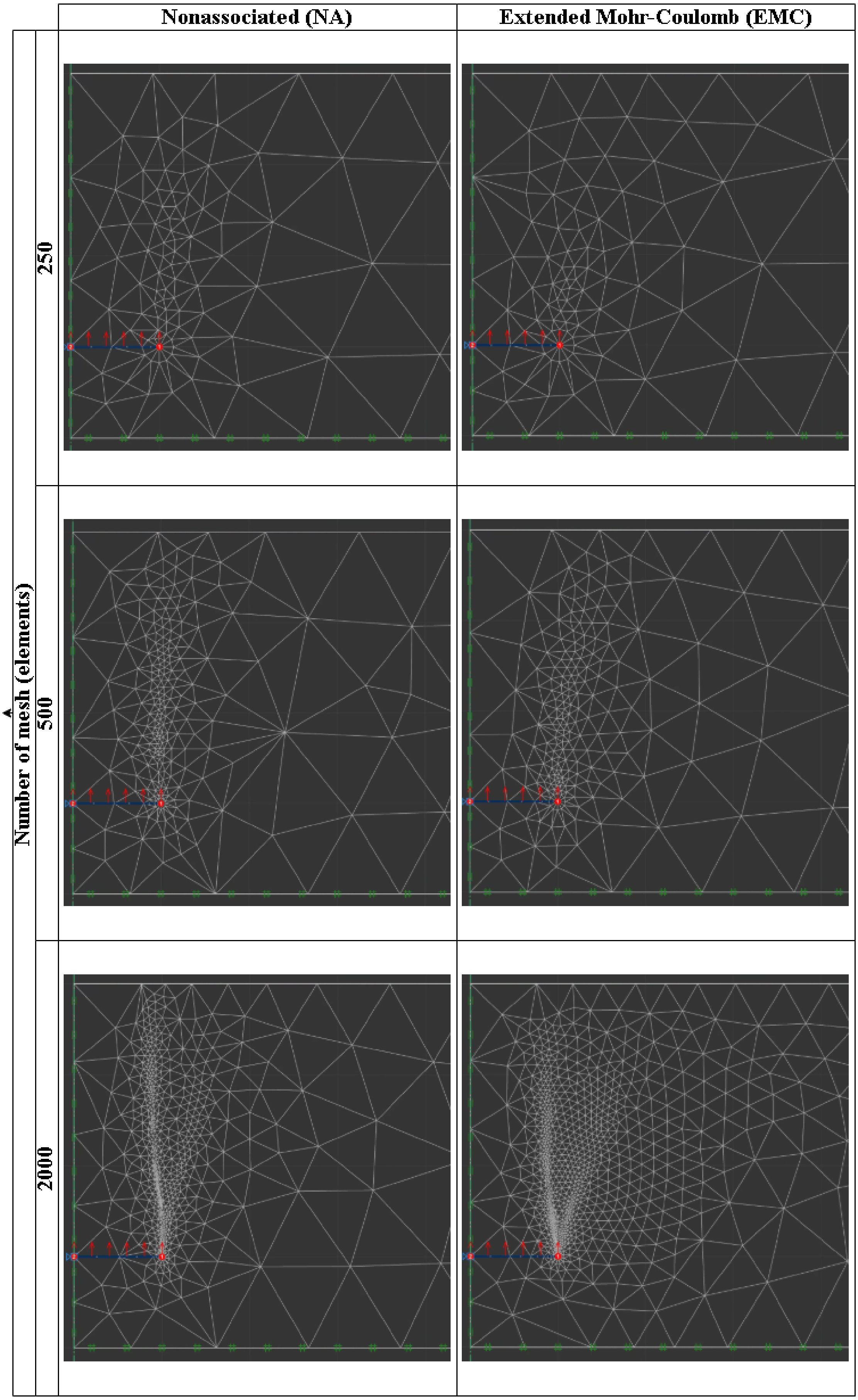

Figure 2.9: Mesh of 250, 500, 2000 elements

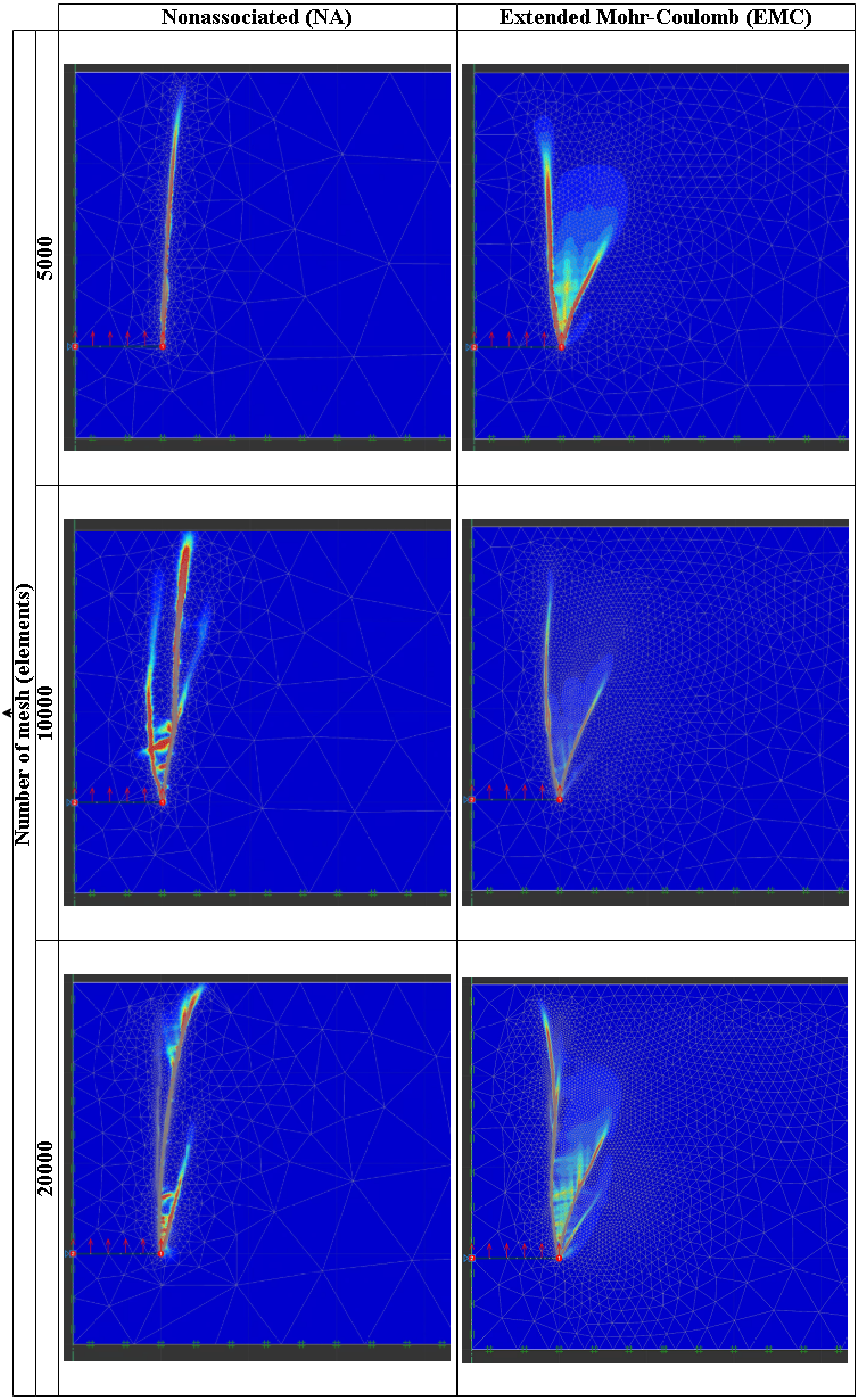

Figure 2.10: Shear Dissipation of the mesh convergence test of 5000, 10000, 20000 elements

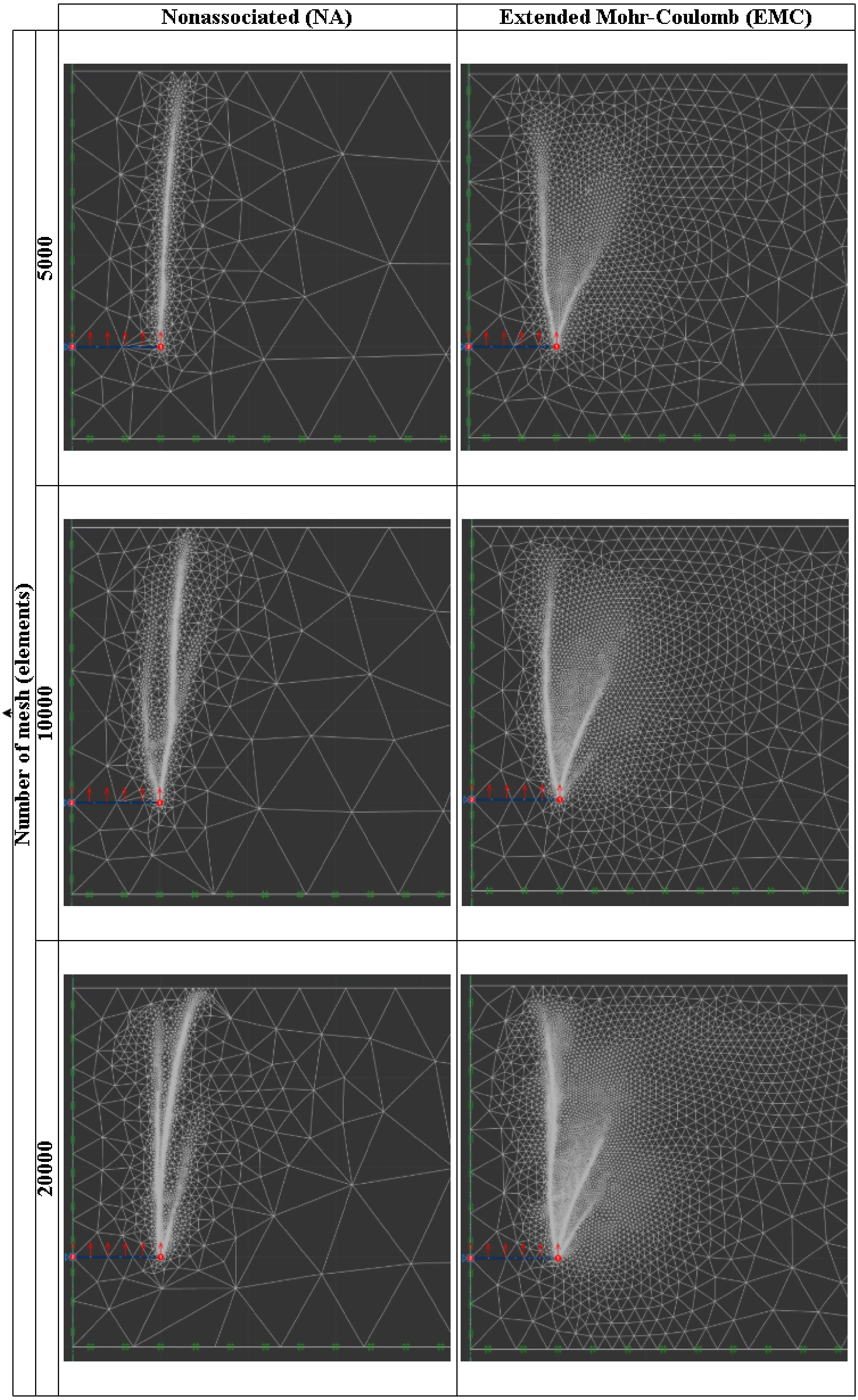

Figure 2.11: Mesh of 5000, 10000, 20000 elements

2.3.2 Boundary Convergence

The soil tank width and the distance below the anchor to the soil tank boundary are the primary condern for the modeling.

Therefore, the optimized value of the soil tank width has been investigated, by differing the values from 10B to 3B, , wherein B refers to the width of the anchor plate.

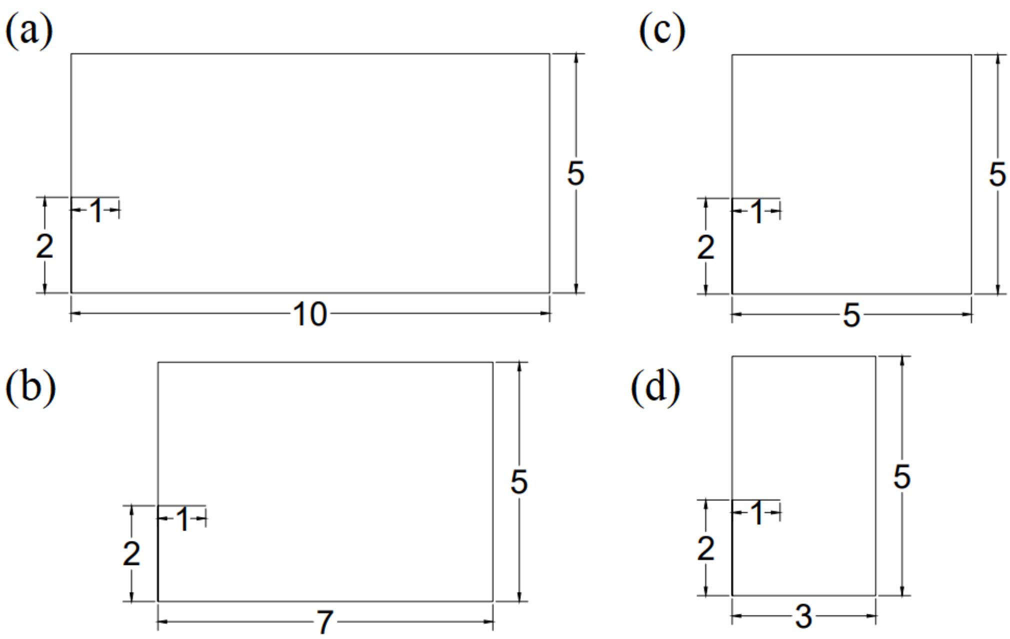

Figure 2.12: Convergence test setup on different boundary size: (a) 10B, (b) 7B, (c) 5B, (d) 3B

Due to the reasoning which considers the method of mesh adaptivity, insignificant effect onto the extension of the soil tank width has been deemed accpetable by the author. Therefore, the result of the boundary convergence test is determined at 10B.

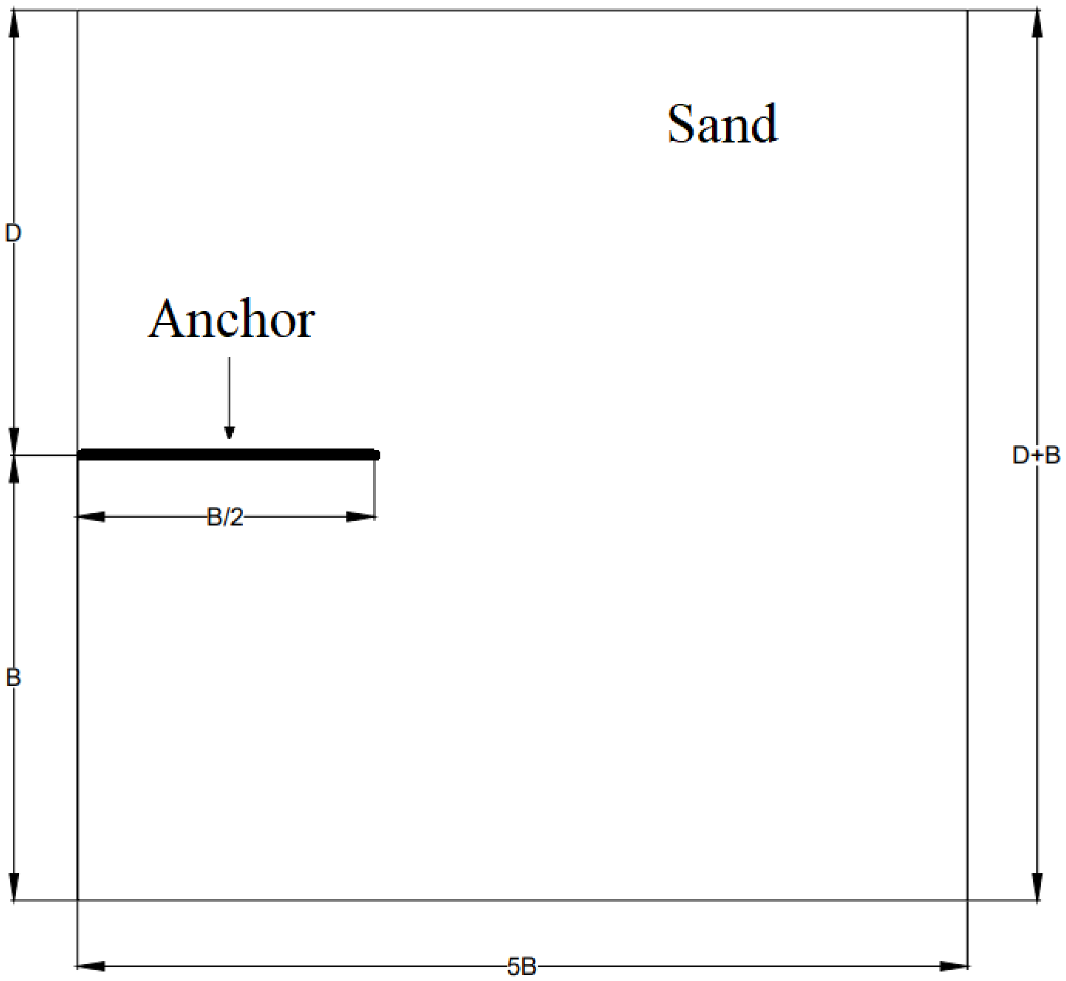

Figure 2.13: Final boundary decision schematic for numerical simulations

Here is a table presenting the setup of boundary convergence test on both NA and EMC models.

Width Boundary	Depth Below Anchor	D/B	Soil Type	Test Type
10B	2B	3	Dense	NA, EMC
7B	2B	3	Dense	NA, EMC
5B	2B	3	Dense	NA, EMC
3B	2B	3	Dense	NA, EMC
10B	2B	3	Medum	NA, EMC
7B	2B	3	Medum	NA, EMC
5B	2B	3	Medum	NA, EMC
3B	2B	3	Medum	NA, EMC
10B	2B	3	Loose	NA, EMC
7B	2B	3	Loose	NA, EMC
5B	2B	3	Loose	NA, EMC
3B	2B	3	Loose	NA, EMC

Table 2.5: Setup of boundary convergence test

Boundary Convergence Results

3

Results

Contents

3.1 Parametric Study

Here is a table presenting the setup of the numerical simulations on both NA and EMC models.

The code refers to the differing width of the plate anchor, , whereas the number specifies if its embedment ratio is either 1,2, or 3.

Code	Test No.	Density	B,m	D,m	D/B
A	LA1	Loose	0.04	0.04	1
B	LB1	Loose	0.2	0.2	1
C	LC1	Loose	1	1	1
D	LD1	Loose	3.5	3.5	1
E	LE1	Loose	4.5	4.5	1
G	LG1	Loose	6.5	6.5	1
A	MA1	Medium	0.04	0.04	1
B	MB1	Medium	0.2	0.2	1
C	MC1	Medium	1	1	1
D	MD1	Medium	3.5	3.5	1
E	ME1	Medium	4.5	4.5	1
G	MG1	Medium	6.5	6.5	1
A	DA1	Dense	0.04	0.04	1
B	DB1	Dense	0.2	0.2	1
C	DC1	Dense	1	1	1
D	DD1	Dense	3.5	3.5	1
E	DE1	Dense	4.5	4.5	1
G	DG1	Dense	6.5	6.5	1
A	LA2	Loose	0.04	0.08	2
B	LB2	Loose	0.2	0.4	2
C	LC2	Loose	1	2	2
D	LD2	Loose	3.5	7	2
E	LE2	Loose	4.5	9	2
G	LG2	Loose	6.5	13	2

Table 3.1 continued from previous page

Code	Test No.	Density	B,m	D,m	D/B
A	MA2	Medium	0.04	0.08	2
B	MB2	Medium	0.2	0.4	2
C	MC2	Medium	1	2	2
D	MD2	Medium	3.5	7	2
E	ME2	Medium	4.5	9	2
G	MG2	Medium	6.5	13	2
A	DA2	Dense	0.04	0.08	2
B	DB2	Dense	0.2	0.4	2
C	DC2	Dense	1	2	2
D	DD2	Dense	3.5	7	2
E	DE2	Dense	4.5	9	2
G	DG2	Dense	6.5	13	2
A	LA3	Loose	0.04	0.12	3
B	LB3	Loose	0.2	0.6	3
C	LC3	Loose	1	3	3
D	LD3	Loose	3.5	10.5	3
E	LE3	Loose	4.5	13.5	3
G	LG3	Loose	6.5	19.5	3
A	MA3	Medium	0.04	0.12	3
B	MB3	Medium	0.2	0.6	3
C	MC3	Medium	1	3	3
D	MD3	Medium	3.5	10.5	3
E	ME3	Medium	4.5	13.5	3

Table 3.1 continued from previous page

Code	Test No.	Density	B,m	D,m	D/B
G	MG3	Medium	6.5	19.5	3
A	DA3	Dense	0.04	0.12	3
B	DB3	Dense	0.2	0.6	3
C	DC3	Dense	1	3	3
D	DD3	Dense	3.5	10.5	3
E	DE3	Dense	4.5	13.5	3
G	DG3	Dense	6.5	19.5	3

Table 3.1: Numerical test setup

3.1.1 Effect of Embedment Depth Ratio $\frac{D}{B}$

Overall Results with All Range of Dense, Medium, Loose Sands

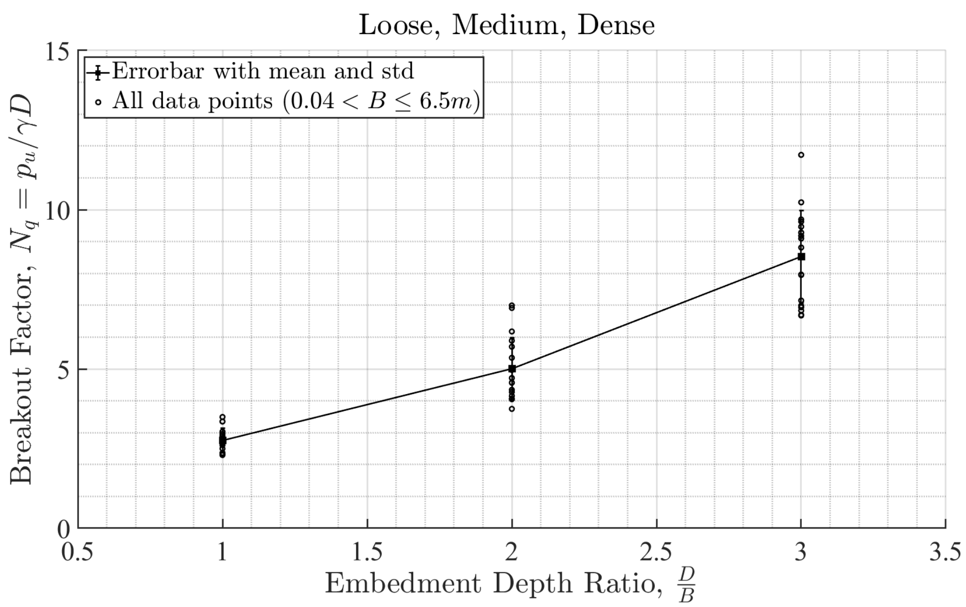

Figure 3.1: Effect of embedment depth ratio on break-out factor for all densities of soil

For Different Sand Densities: *Loose, Medium, Dense*

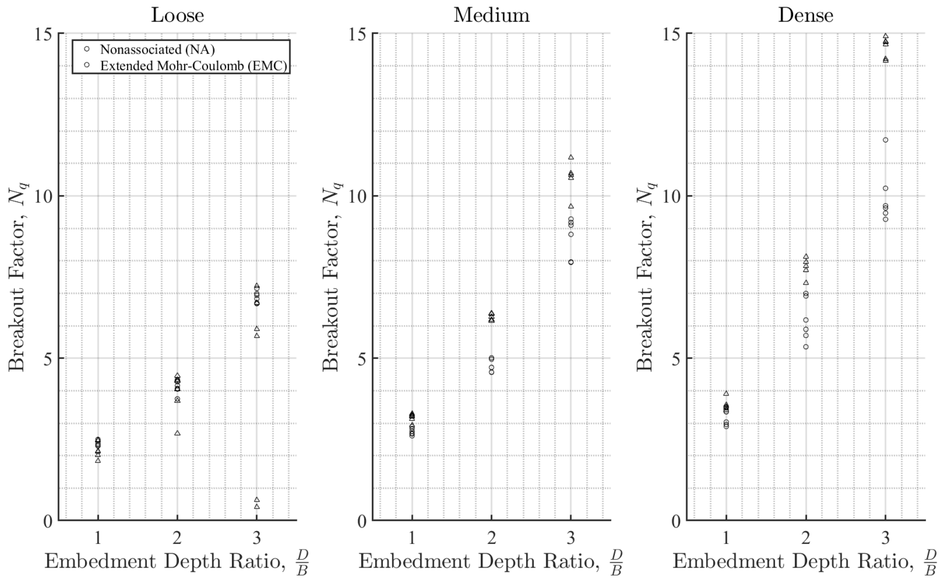

Figure 3.2: Effect of embedment depth ratio on break-out factor (a) loose (b) medium (c) dense

3.1.2 Effect of Width B

Overall Results with All Range of Dense, Medium, Loose Sands

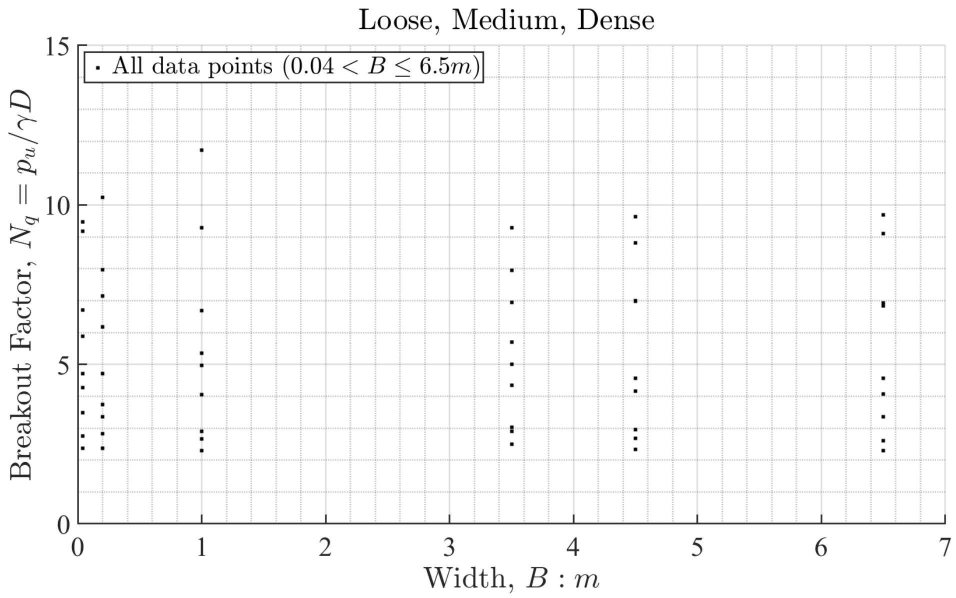

Figure 3.3: Effect of width of plate for all densities of soil

3.1.3 Shear Dissipation

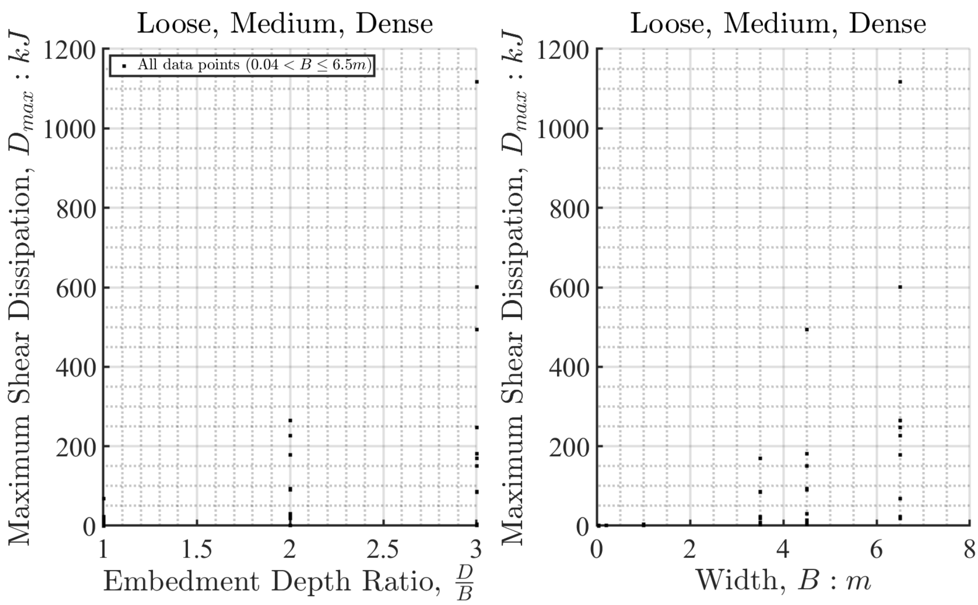

Figure 3.4: Effect of embedment depth and width on shear dissipation for all densities of soil

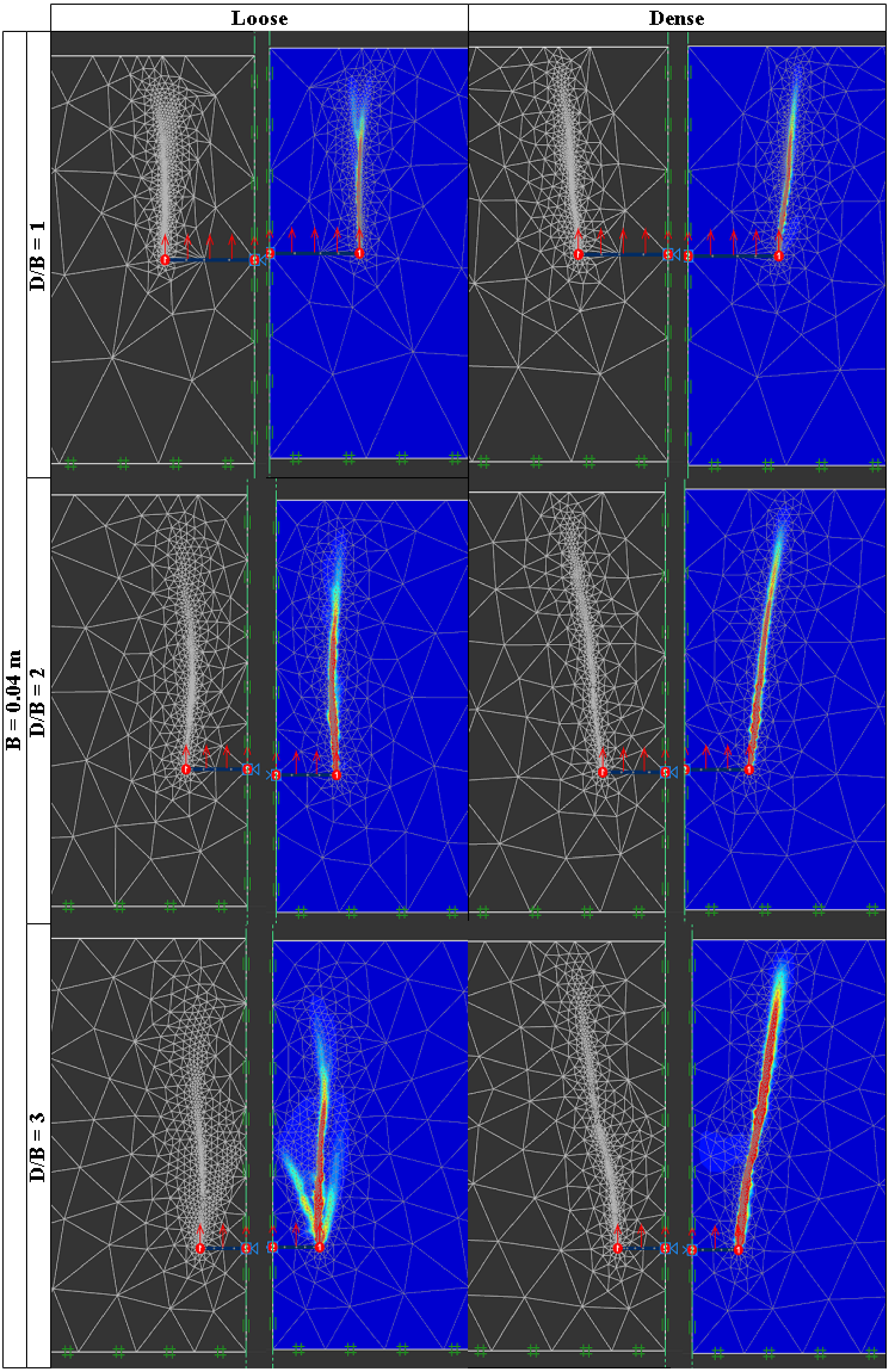

Figure 3.5: Shear dissipation of NA model at 10 percent of the maximum value and $B = 0.04m$

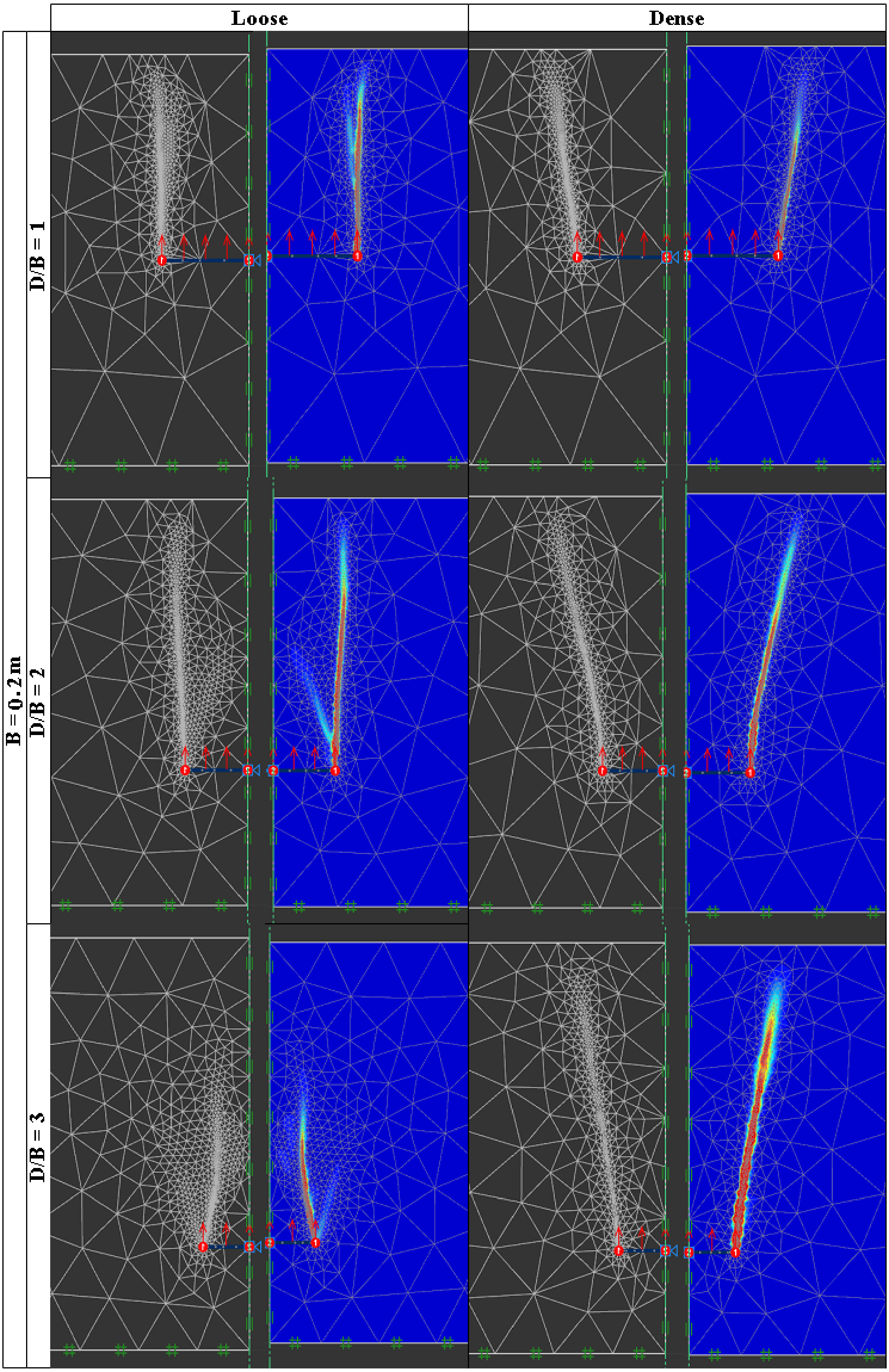

Figure 3.6: Shear dissipation of NA model at 10 percent of the maximum value and $B = 0.2m$

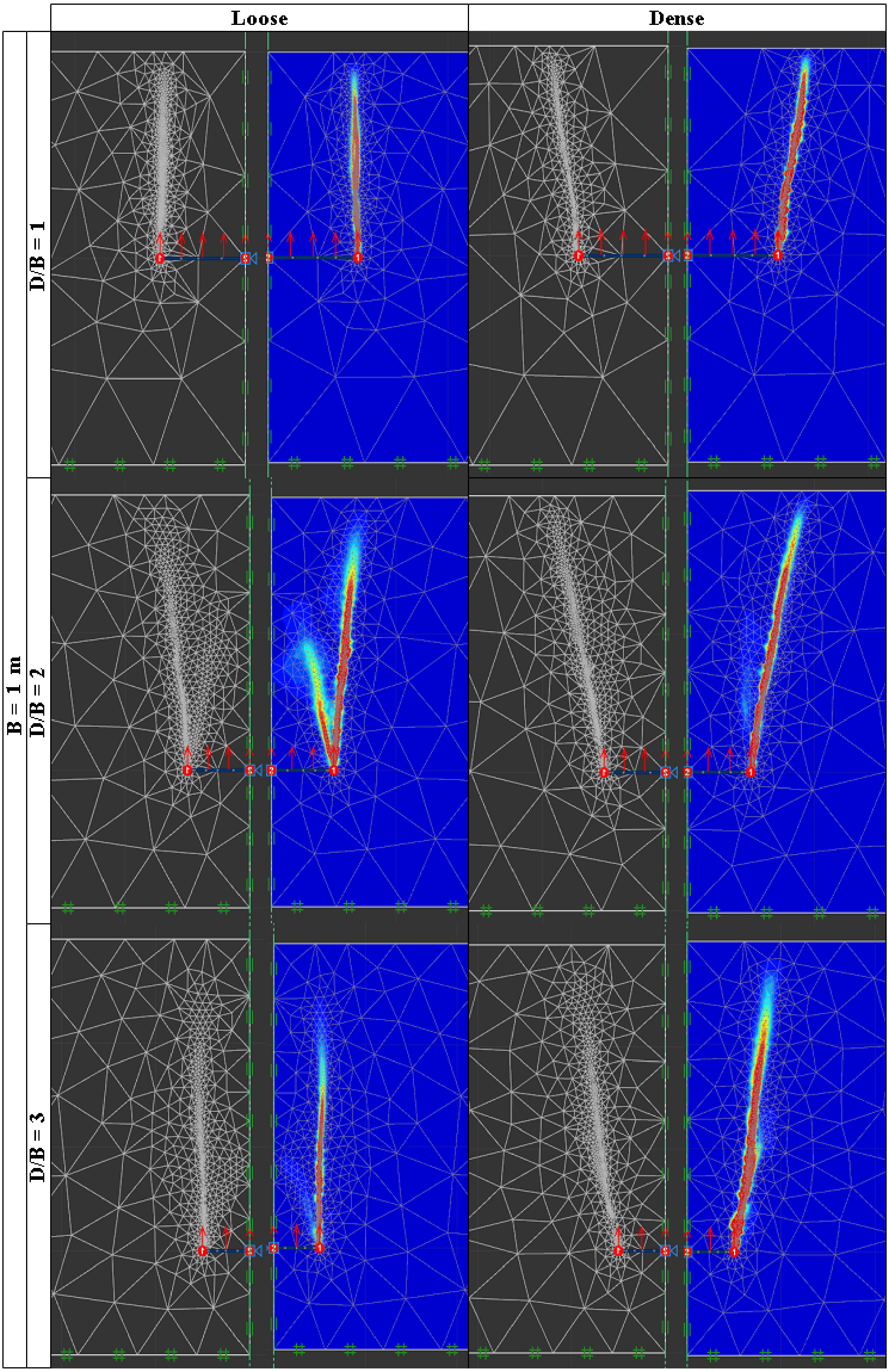

Figure 3.7: Shear dissipation of NA model at 10 percent of the maximum value and $B = 1.0m$

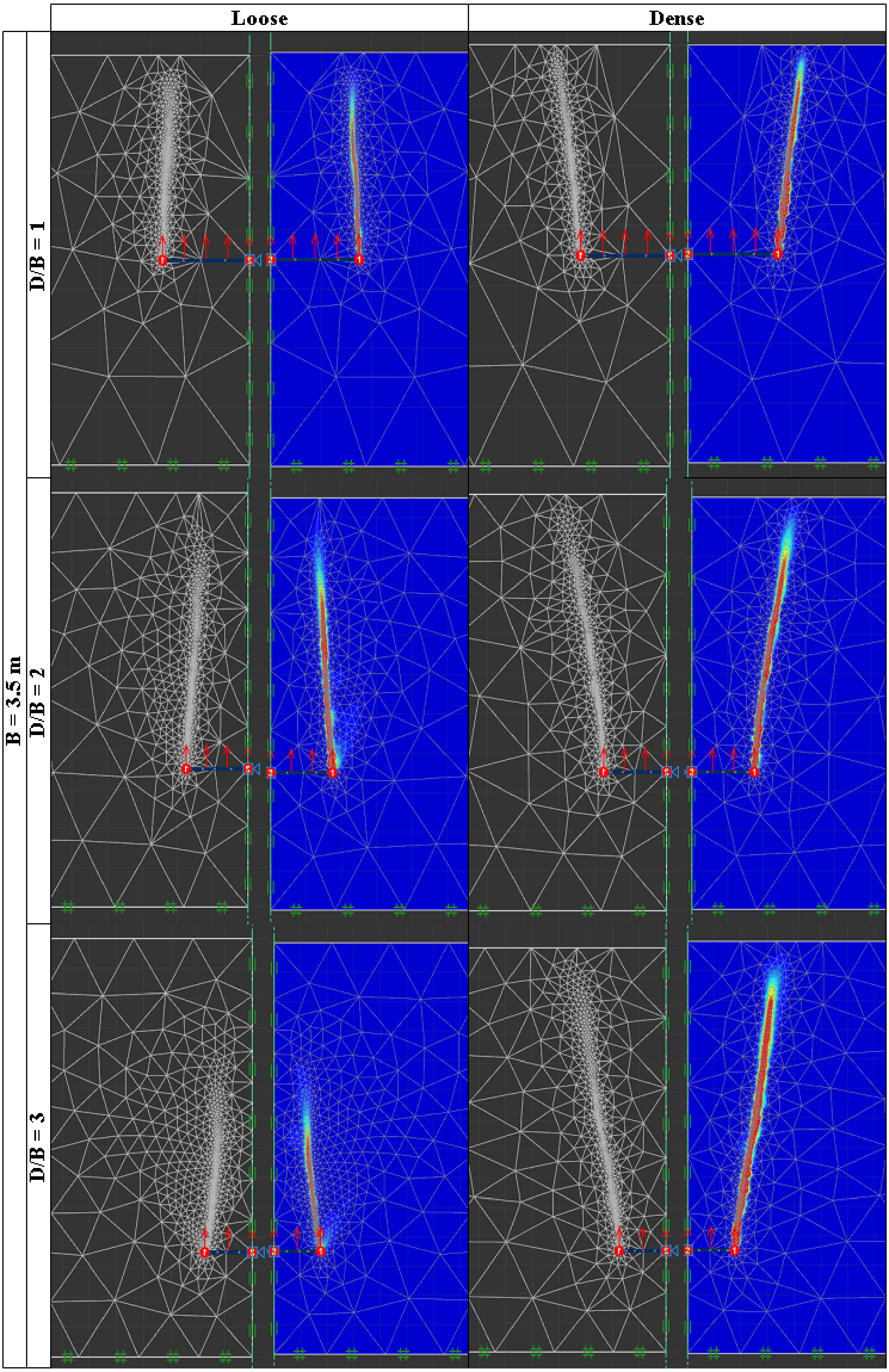

Figure 3.8: Shear dissipation of NA model at 10 percent of the maximum value and $B = 3.5m$

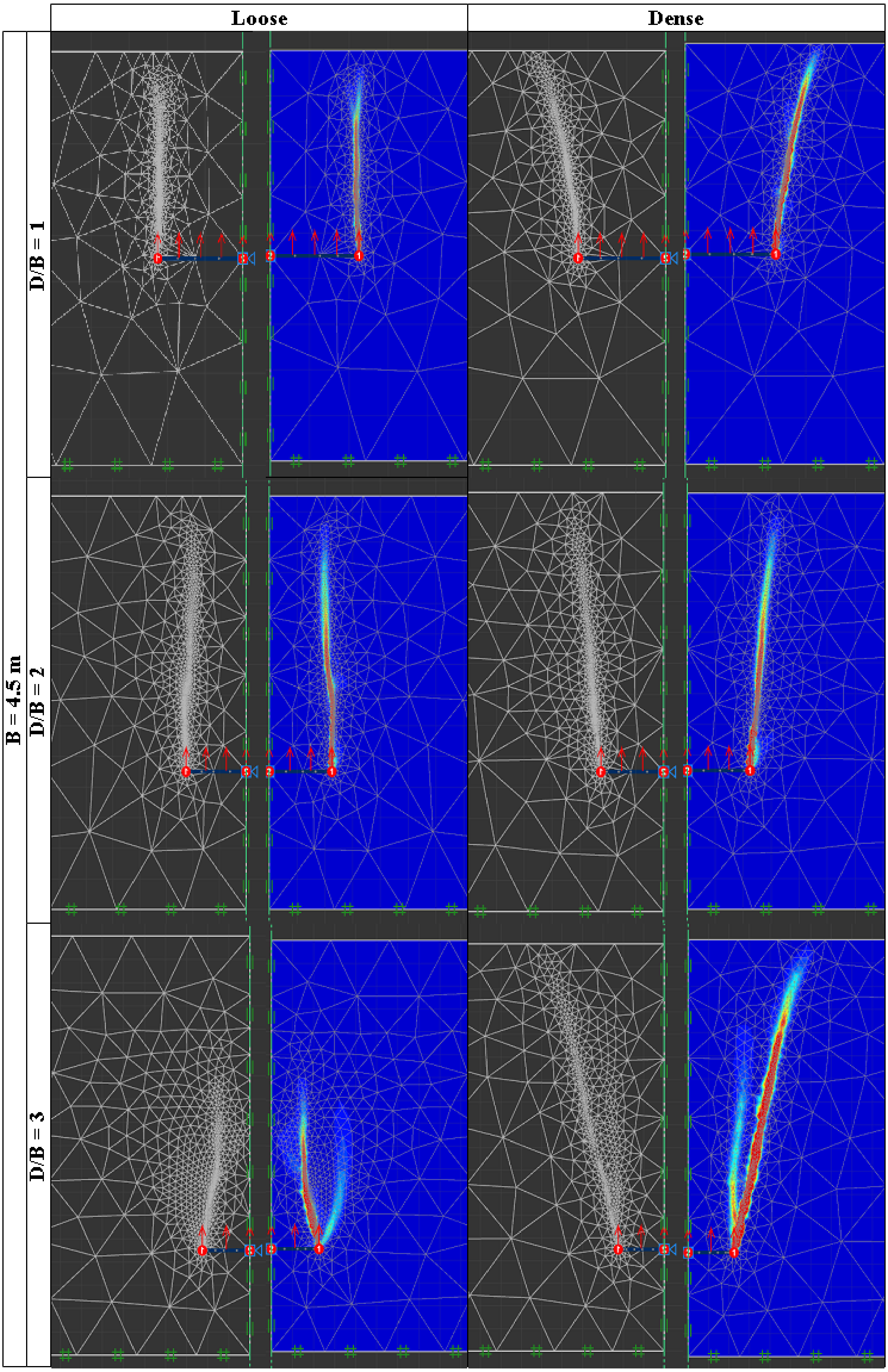

Figure 3.9: Shear dissipation of NA model at 10 percent of the maximum value and $B = 4.5m$

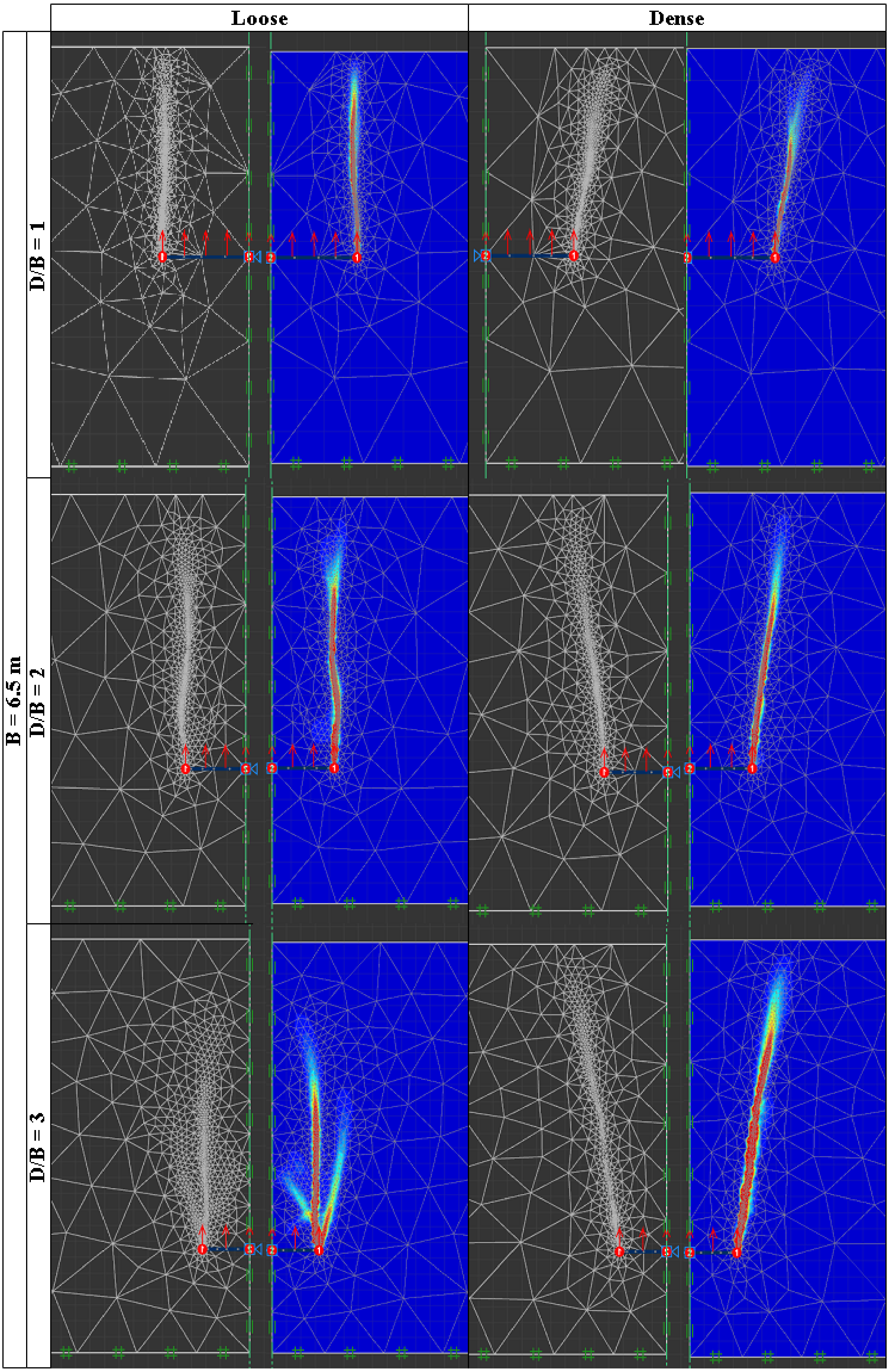

Figure 3.10: Shear dissipation of NA model at 10 percent of the maximum value and $B = 6.5m$

3.2 Comparison with Previous Researchers

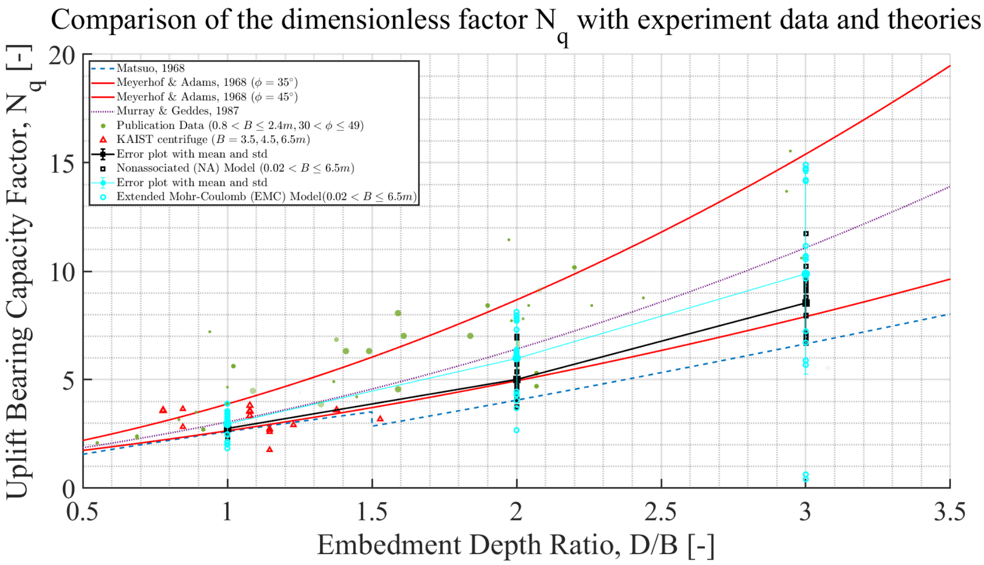

Figure 3.11: Comparison with theories and experimental data in all densities of sands

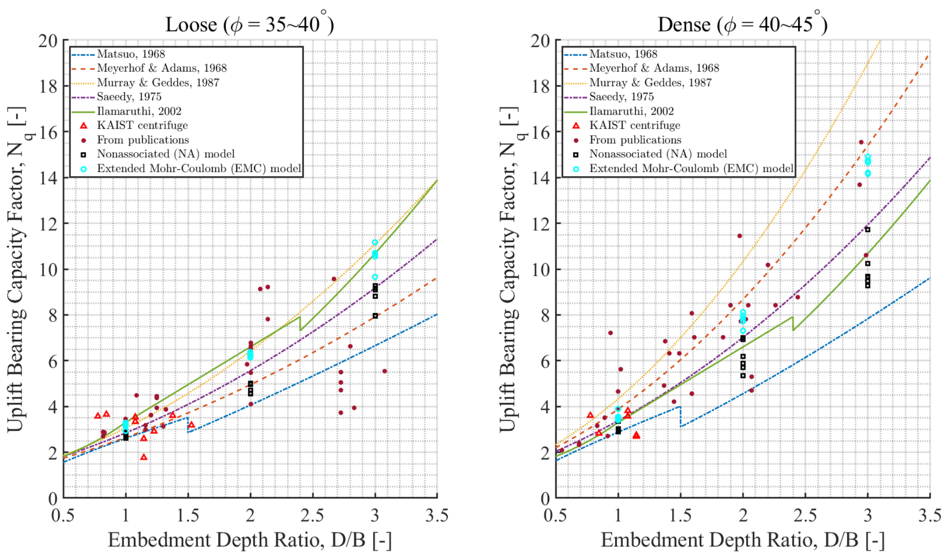

Figure 3.12: Comparison with theories and experimental data in loose and dense sands

Comparison of the plot of the effect of width on resistance

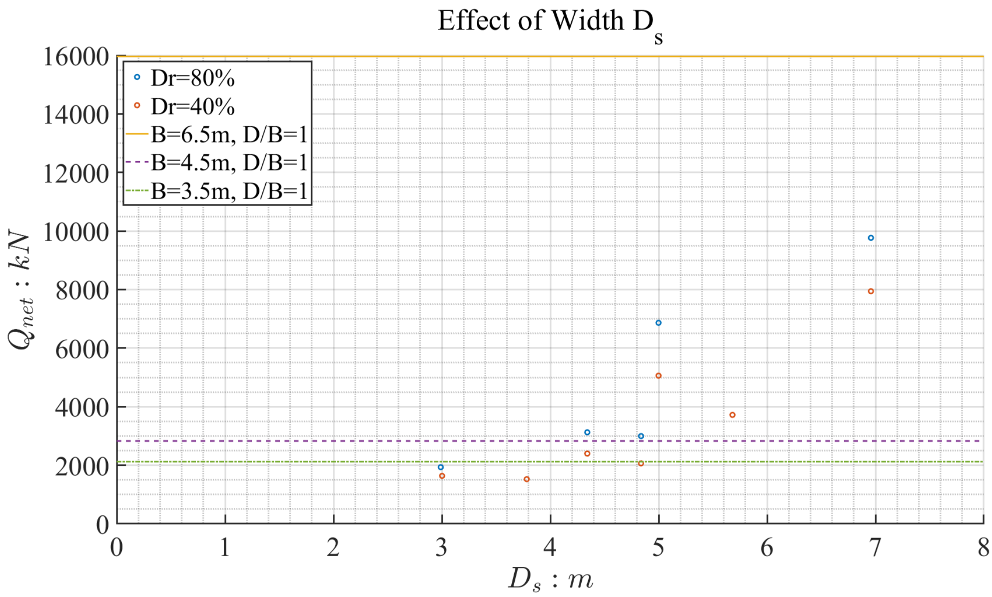

Figure 3.13: Comparison drawn

Appendices

A

Nomenclature

a, b, m are soil parameters,

$p^{'}$ is mean stress,

J_2 is second invariant of deviatoric stress,

χ is a soil parameter,

$c(\chi)$ is apparent cohesion function

$\delta\varepsilon^p_{x,y,z}, \delta\gamma^p$ is incremental deviatoric plastic strains

θ is Lode angle,

ϕ is mobilized internal friction angle,

$\phi_{p,r}$ are peak and residual friction angle, respectively.

ν Poisson's ratio

ν void ratio

G_0 initial shear modulus

β and ϵ_d are stress–dilatency material parameters.

$\eta_{y,p}$ is stress ratio at yield and peak, respectively,

p_r' is chosen so that plastic potential gradient passes through current stress point

β and ϵ_d are stress–dilatency material parameters.

E_{50} is a secant modulus defined as:

$E_{50} = \frac{\frac{1}{2} q_u}{\varepsilon_{a,50}}$

E_{ur} is unloading/reloading stiffness.

ν is Poisson's ratio

e is void ratio

G_0 is initial shear modulus.

B

List of Load—Displacement Curves

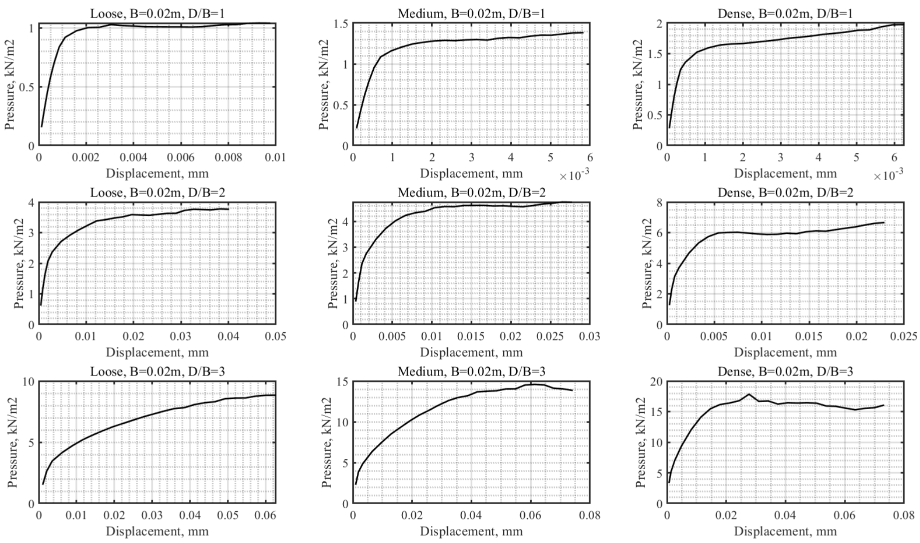

Figure B.1: Cumulative load-displacement curves of uplift of plate anchor in loose, medium, dense sands; D/B = 1,2,3; B=0.02m

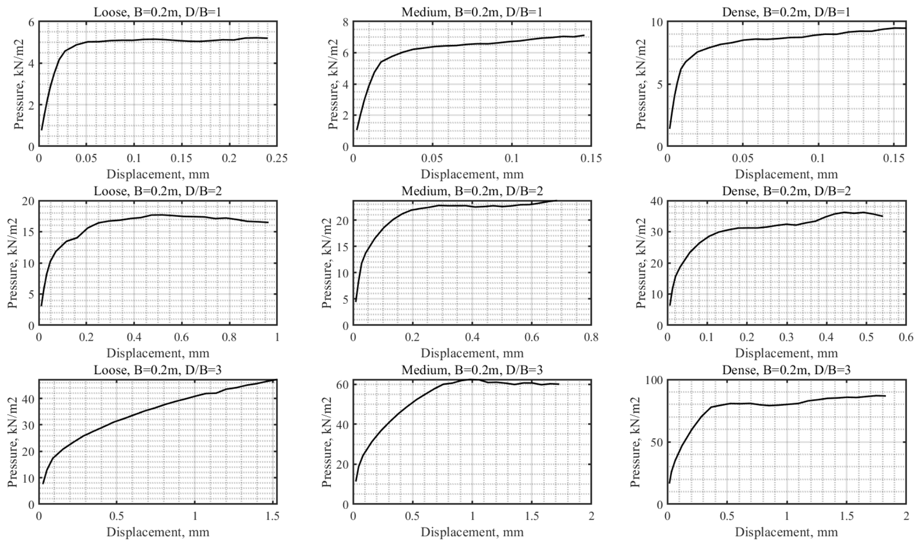

Figure B.2: Cumulative load-displacement curves of uplift of plate anchor in loose, medium, dense sands; D/B = 1,2,3; B=0.2m

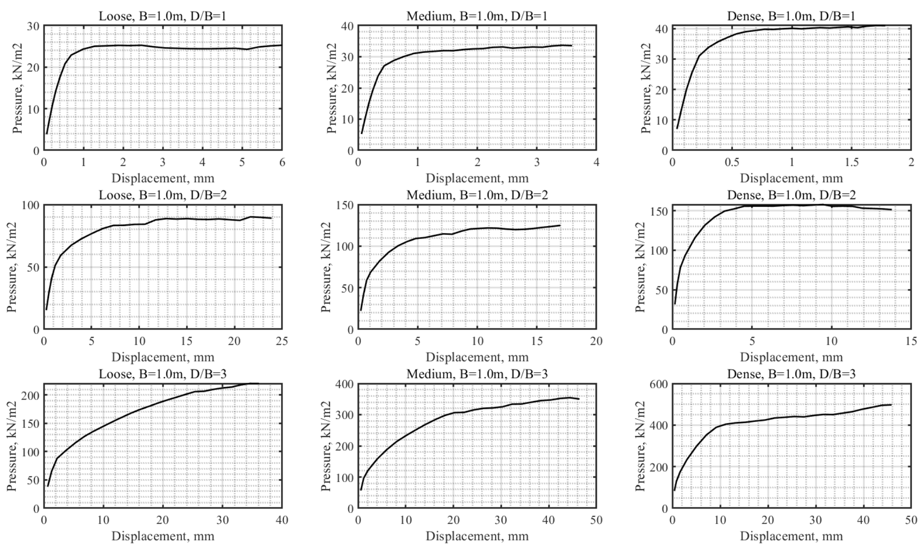

Figure B.3: Cumulative load-displacement curves of uplift of plate anchor in loose, medium, dense sands; D/B = 1,2,3; B=1.0m

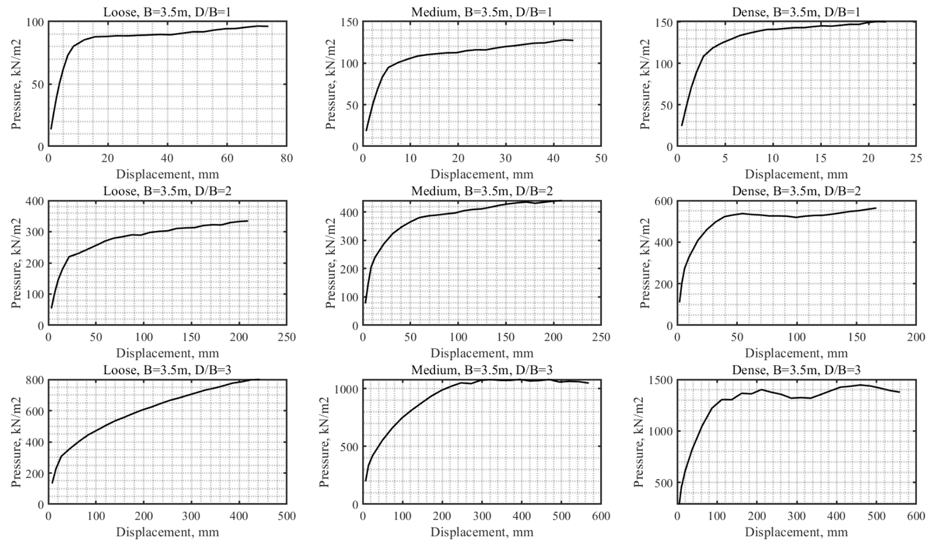

Figure B.4: Cumulative load-displacement curves of uplift of plate anchor in loose, medium, dense sands; D/B = 1,2,3; B=3.5m

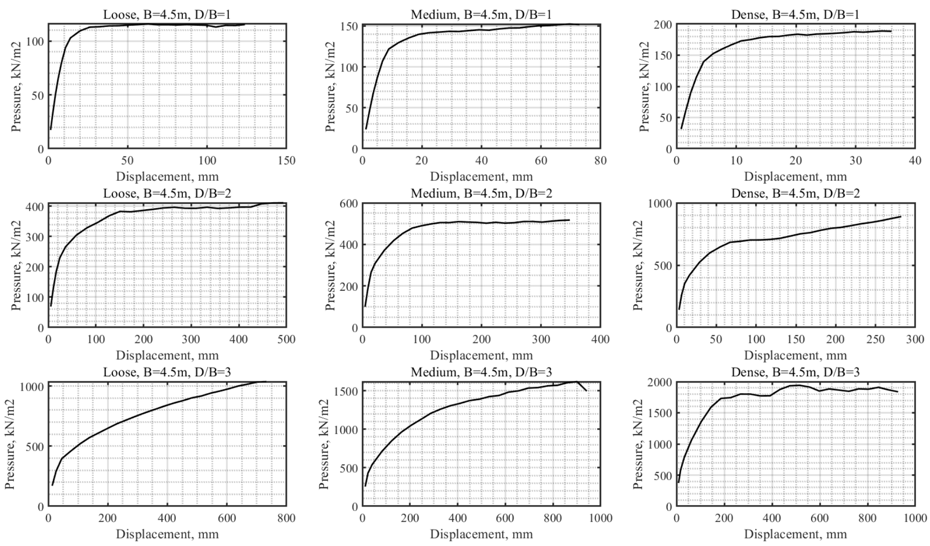

Figure B.5: Cumulative load-displacement curves of uplift of plate anchor in loose, medium, dense sands; D/B = 1,2,3; B=4.5m

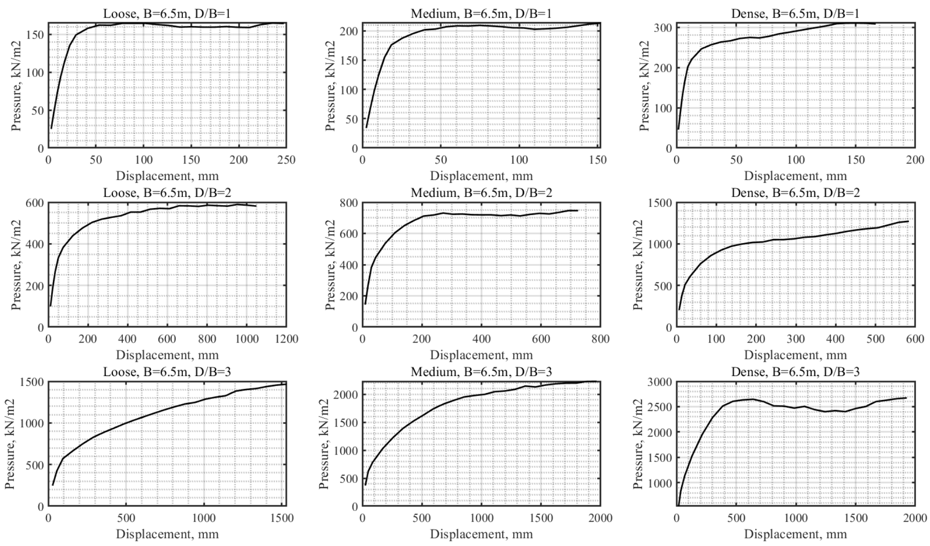

Figure B.6: Cumulative load-displacement curves of uplift of plate anchor in loose, medium, dense sands; D/B = 1,2,3; B=6.5m

REFERENCES

Wood, D. M. (2017). Geotechnical modelling. CRC press.

Doherty, J. P., & Muir Wood, D. (2013). An extended Mohr–Coulomb (EMC) model for predicting the settlement of shallow foundations on sand. Géotechnique, 63(8), 661-673.

Gajo, A., & Wood, M. (1999). Severn–Trent sand: a kinematic-hardening constitutive model: the q–p formulation. Géotechnique, 49(5), 595-614.

Krabbenhoft, S., Krabbenhoft, K., & Christensen, R. Limit analysis of the bearing capacity of strip-and circular footings on a layer of sand overlying clay.

Sakai, T., & Tanaka, T. (2007). Experimental and numerical study of uplift behavior of shallow circular anchor in two-layered sand. Journal of geotechnical and geoenvironmental engineering, 133(4), 469-477.

Tanaka, T., & Sakai, T. (1993). Progressive failure and scale effect of trap-door problems with granular materials. Soils and Foundations, 33(1), 11-22.

Sakai, T., & Tanaka, T. (1998). Scale effect of a shallow circular anchor in dense sand. Soils and Foundations, 38(2), 93-99.

Sakai, T., & Tanaka, T. (2007). Experimental and numerical study of uplift behavior of shallow circular anchor in two-layered sand. Journal of geotechnical and geoenvironmental engineering, 133(4), 469-477.

Riyad, A. S. M., Rokonuzzaman, M., & Sakai, T. (2020). Progressive failure and scale effect of anchor foundations in sand. Ocean Engineering, 195, 106496.

Kumar, J., & Kouzer, K. M. (2008). Vertical uplift capacity of horizontal anchors using upper bound limit analysis and finite elements. Canadian Geotechnical Journal, 45(5), 698-704.

Riyad, A. S. M., Rokonuzzaman, M., & Sakai, T. (2020). Effect of using different approximation models to the exact Mohr–Coulomb material model in the FE simulation of Anchor Foundations in sand. International Journal of Geo-Engineering, 11(1), 1-21.

Riyad, A. S. M., Rokonuzzaman, M., & Sakai, T. (2020). Progressive failure and scale effect of anchor foundations in sand. Ocean Engineering, 195, 106496.

Roy, A., Chow, S. H., O'Loughlin, C. D., & Randolph, M. F. (2021). Towards a simple and reliable method for calculating uplift capacity of plate anchors in sand. Canadian Geotechnical Journal, 58(9), 1314-1333.